



ALE method for solidification modelling

Michel Bellet, Victor D. Fachinotti

► To cite this version:

Michel Bellet, Victor D. Fachinotti. ALE method for solidification modelling. Computer Methods in Applied Mechanics and Engineering, 2004, 193 (39-41), p. 4355-4381. 10.1016/j.cma.2003.11.016 . hal-00531192

HAL Id: hal-00531192

<https://hal-mines-paristech.archives-ouvertes.fr/hal-00531192>

Submitted on 11 Mar 2011

HAL is a multi-disciplinary open access archive for the deposit and dissemination of scientific research documents, whether they are published or not. The documents may come from teaching and research institutions in France or abroad, or from public or private research centers.

L'archive ouverte pluridisciplinaire **HAL**, est destinée au dépôt et à la diffusion de documents scientifiques de niveau recherche, publiés ou non, émanant des établissements d'enseignement et de recherche français ou étrangers, des laboratoires publics ou privés.

ALE method for solidification modelling

Michel Bellet, Victor D. Fachinotti

Ecole des Mines de Paris, Centre de Mise en Forme des Matériaux (CEMEF), UMR CNRS 7635, BP 207, F-06904 Sophia Antipolis, France. E-mail: michel.bellet@ensmp.fr

Abstract

In this paper an arbitrary Lagrangian-Eulerian (ALE) formulation has been developed for the simulation of casting processes. The method is applied both to mould filling simulation, where it can provide accurate free surface description, and to the study of thermomechanical phenomena occurring in the subsequent cooling down of cast parts: prediction of solute transport and of distortions and stresses. In the first three sections, all governing equations (constitutive equations, momentum, energy, solute transport) are given. Then the ALE formulation is presented: mesh updating with evolving free surfaces, using “conservative” normal vectors to enforce mass conservation ; treatment of advection terms, using an original nodal upwind method ; definition of Lagrangian and Eulerian-Lagrangian regions. Finally, examples of applications are given.

Keywords

ALE - finite elements – casting simulation – mould filling - solidification

NOTATIONS

g_l	volumetric liquid fraction (-)
g_s	volumetric solid fraction (-)
H	strain hardening coefficient (-)
k	partition coefficient (-)
K	viscoplastic consistency (Pa.s ^m)
m	strain-rate sensitivity index (-)
n	strain hardening exponent (-)
\mathbf{P}	vector of nodal pressures (Pa)
$p = -\frac{1}{3} \text{tr } \boldsymbol{\sigma}$	pressure (Pa)
$\mathbf{s} = \boldsymbol{\sigma} + p\mathbf{I}$	deviatoric stress tensor (Pa)
\mathbf{T}	stress vector (Pa)
\mathbf{V}	vector of nodal velocities (m.s ⁻¹)
\mathbf{v}	velocity vector (m.s ⁻¹)
w	average solute concentration in the solid-liquid mixture (mass%)
w^l	average solute concentration in the liquid phase (mass%)
w^s	average solute concentration in the solid phase (mass%)
\mathbf{X}	vector of nodal spatial coordinates (m)
β_w	solatal expansion coefficient (1/%solute)
$\Delta\epsilon^{tr} = \frac{\rho(T_L) - \rho(T_S)}{\rho(T_L)} < 0$	shrinkage ratio: relative volume change associated with the total liquid-solid transition (-)
ϵ	solute diffusivity (m ² .s ⁻¹)
$\dot{\epsilon}$	strain rate tensor, or symmetric part of the tensor of velocity gradients (s ⁻¹)
$\dot{\epsilon}^{el}$	elastic part of the strain rate tensor (s ⁻¹)
$\dot{\epsilon}^{vp}$	viscoplastic part of the strain rate tensor (s ⁻¹)
$\dot{\epsilon}^{th}$	thermal part of the strain rate tensor (s ⁻¹)
$\dot{\epsilon}_{eq} = \sqrt{\frac{2}{3} \dot{\epsilon}_{ij}^{vp} \dot{\epsilon}_{ij}^{vp}}$	von Mises equivalent plastic strain-rate (s ⁻¹)

$$\varepsilon_{eq} = \int_0^t \dot{\varepsilon}_{eq} dt$$

von Mises equivalent plastic strain (-)

μ

dynamic viscosity of the liquid (Pa.s or kg.m⁻¹.s⁻¹)

σ

Cauchy stress tensor (Pa)

$$\sigma_{eq} = \sqrt{\frac{3}{2} s_{ij} s_{ij}}$$

von Mises equivalent stress (Pa)

σ_0

static yield stress (Pa) (plastic threshold : if $\sigma_{eq} < \sigma_0$, the material is elastic)

σ_{00}

initial static yield stress (elasticity limit) (Pa)

1. Introduction : the ALE formulation in the context of solidification processes

The paper presents two different examples of the use of Arbitrary Lagrangian-Eulerian (ALE) formulation in the context of the casting of metal alloys.

First, ALE can be used for mould filling simulations, which are carried out in order to provide the downstream thermomechanical and microstructural computations of the cooling stage with accurate initial conditions in terms of temperature and velocity field. Additionally, they can help in understanding the occurrence of defects such as incomplete filling due to early solidification, convection of inclusions, oxidation associated with turbulence, mould wear, etc. Most mould filling models are of fixed mesh type. This is of course the most convenient way to approach non steady state fluid flow since the computation grid can remain fixed from the beginning to the end of the filling. One of the main issues is then the tracking of the free surface separating the fluid domain from the rest of the mould cavity. Most codes use the volume of fluid (VOF) method, see for instance the works of Bourg *et al* [1], Barkhudarov *et al* [2] ; Waite and Samonds [3] ; Codina *et al* [4]; Lewis *et al* [5]; Mampey and Xu [6]; Zhu and Ohnaka [7]; Médale and Jaeger [8]; and the documentation on Magmasoft and Procast software [9-10]. The VOF method [11] consists in solving the conservation equation $dF/dt = 0$ for a variable F – the volumic fraction of fluid – whose value is one in filled regions and zero elsewhere. Two fluids are actually considered: the molten alloy and a gas in the empty regions. This method suffers generally from numerical diffusion in the resolution of the free surface tracking equation, which is of pure advective type. The precision of the computation is strongly dependent on the mesh density. This implies that in case of complex flow the user must have *a priori* a fairly good idea of the liquid flow in order to capture properly the critical features of the flow. In addition, the method can hardly handle the discontinuity of the material viscosity at the interface. To prevent this difficulty, the viscosity value is smoothed around the interface, adding once again some inaccuracy. Since the value $F = 1/2$ is supposed to represent the free surface, it results in a smeared fluid surface. An alternative to the fixed mesh methods are the methods in which the mesh covers the fluid domain only, as proposed by Navti and Lewis [12-13], or Gaston and Bellet [14]. Based on updated Lagrangian schemes, they must be associated with the ALE formulation in order to reduce the number of full remeshing operations. In this paper, we will give an example of application of such an ALE method to the two-dimensional simulation of mould filling.

The ALE method is also very useful in the second step of solidification analysis. After mould filling and during the cooling down and the progressive solidification of a cast part, the remaining liquid pools can be affected by convection caused by the density gradients. Convection can be initiated at high Rayleigh numbers, *i.e.* when the cast parts are large enough. The gradients of density can be caused by gradients of temperature and alloy elements concentration. When considering a constant density in the source term of the momentum equation, this thermal and solutal convection phenomena are neglected and liquid pools remain more or less quasi static along the computation. This approximation is acceptable in the case of small parts or for larger ones when liquid convection is neglected as a first approach (the temperature homogenization associated with

liquid convection is simply not captured by the simulation). In this case, the fluid motion is originated by the alloy volumetric contraction during phase change and cooling. Conversely, when we use a density depending on the local temperature and alloy concentration, convection effects are accounted for. In this case, and provided that the Rayleigh number be high enough, the velocity in the liquid regions are significantly higher than those of the solid regions. In both cases, and especially in the second one, the fluid motion cannot be handled with a classical updated Lagrangian scheme, since it would lead to mesh degeneracy in the liquid pools. At the same time, a purely Eulerian scheme is not satisfying, since it cannot provide enough accuracy for the motion of the free surfaces of the solidified regions of the part: the location of the physical boundary of the part by a front tracking algorithm is irrelevant when dealing with air gap opening between part and mould for instance. Therefore, the ALE formulation appears very attractive to solve this kind of problems.

Jaouen and Bellet have implemented and developed the ALE method in the finite element code THERCAST[®] dedicated to solidification analysis [15-17]. THERCAST[®] addresses the three-dimensional thermomechanical analysis of castings during their solidification. The code is developed by CEMEF and TRANSVALOR and is focused on the calculation of deformations and stresses in the castings (taking into account possible deformations of moulds) and on the calculation of the macrosegregation of alloying elements. An equivalent two-dimensional software, named R2SOL, has approximately the same characteristics as THERCAST[®], besides the ability to address mould filling analysis.

The outline of the paper will be as follows. The next three sections will present the conservation equations for momentum, energy and solutes and the finite element resolution which prevail in these two finite element codes. Then the main issues of ALE implementation in the solidification context will be discussed. Finally, examples of application will be presented.

2. Mechanical problem: governing equations and finite element resolution

2.1 Constitutive equations for metallic alloys in solidification conditions

A detailed discussion regarding this point can be found in [17]. Here the main ideas of the approach used by the authors are briefly reminded. The reader is also invited to refer to the nomenclature section for the notations used, except the most standard ones which will be incorporated into the text.

A metallic alloy in liquid or mushy state is modelled using a pure thermo-viscoplastic law, without any elastic contribution. Depending on the temperature (or the solid fraction), the model is either purely Newtonian (pure liquid state) or non linear viscoplastic (mushy state). Below a critical temperature T_C (for instance the “coherency” temperature or the solidus temperature), the alloy behaviour is modelled by a thermo-elastic-viscoplastic constitutive law, which is more representative of solid-like behaviour.

2.1.1 Liquid-like constitutive equations: pure thermo-viscoplastic model

In this case, the compressibility is only due to the thermal contribution (no elasticity). The equations of the constitutive model can be written as follows.

$$\begin{cases} \dot{\boldsymbol{\varepsilon}} = \dot{\boldsymbol{\varepsilon}}^{vp} + \dot{\boldsymbol{\varepsilon}}^{th} \\ \dot{\boldsymbol{\varepsilon}}^{vp} = \frac{1}{2K} \left(\sqrt{3} \dot{\boldsymbol{\varepsilon}}_{eq} \right)^{1-m} \mathbf{s} \\ \dot{\boldsymbol{\varepsilon}}^{th} = \left(\alpha \dot{T} + \frac{1}{3} \dot{g}_s \Delta \boldsymbol{\varepsilon}^{tr} \right) \mathbf{I} \end{cases} \quad (1)$$

In this set of equations, α denotes the thermal linear expansion coefficient, \mathbf{I} the identity tensor and \dot{T} the time derivative of temperature. The strain rate tensor is split into a viscoplastic, and a thermal part (1a). The latter includes thermal expansion and shrinkage due to the liquid-solid phase change (1c). Equation (1b) is the classical constitutive equation of a generalized non Newtonian fluid. It relates the viscoplastic strain rate to the stress deviator. The limit case of the Newtonian behaviour (liquid state) is obtained for $m = 1$. In this case, K is simply the dynamic viscosity of the liquid.

2.1.2 Solid-like constitutive equations: thermo-elastic-viscoplastic model

The model used to represent the solidifying material behaviour below T_C is described by the following equations:

$$\begin{cases} \dot{\boldsymbol{\varepsilon}} = \dot{\boldsymbol{\varepsilon}}^{el} + \dot{\boldsymbol{\varepsilon}}^{vp} + \dot{\boldsymbol{\varepsilon}}^{th} \\ \dot{\boldsymbol{\varepsilon}}^{el} = \frac{1+\nu}{E} \dot{\boldsymbol{\sigma}} - \frac{\nu}{E} \text{tr}(\dot{\boldsymbol{\sigma}}) \mathbf{I} \\ \dot{\boldsymbol{\varepsilon}}^{vp} = \frac{\sqrt{3}}{2\sigma_{eq}} \left\langle \frac{\sigma_{eq} - \sigma_0 - H\boldsymbol{\varepsilon}_{eq}^n}{K\sqrt{3}} \right\rangle^{1/m} \mathbf{s} \\ \dot{\boldsymbol{\varepsilon}}^{th} = \left(\alpha \dot{T} + \frac{1}{3} \dot{g}_s \Delta \boldsymbol{\varepsilon}^{tr} \right) \mathbf{I} \end{cases} \quad (2)$$

Here E and ν are the usual notations for Young's modulus and Poisson's coefficient. For less standard notations, see the nomenclature section. The strain rate tensor is split in an elastic, a viscoplastic, and a thermal part (2a). As in the fluid-like model, the latter includes thermal expansion and shrinkage due to the liquid-solid phase change (2d or 1c). Equation (2b) yields the hypoelastic Hooke's law. Equation (2c) gives the relation between the viscoplastic strain rate and the stress deviator, in which $\sigma_0 = \sigma_0 + H\boldsymbol{\varepsilon}_{eq}^n$ denotes the static yield stress below which no viscoplastic deformation occurs (the expression between Macauley brackets $\langle \rangle$ is reduced to zero when negative).

When multidomain calculations are carried out with THERCAST[®], the set of equations (2) is used to model the thermo-elastic-viscoplastic behaviour of mould materials.

2.2 Momentum equation

At any time, the local momentum conservation is expressed by:

$$\nabla \cdot \boldsymbol{\sigma} + \rho \mathbf{g} - \rho \boldsymbol{\gamma} = \nabla \cdot \mathbf{s} - \nabla p + \rho \mathbf{g} - \rho \boldsymbol{\gamma} = 0 \quad (3)$$

where ρ denotes the specific mass (or “density”), \mathbf{g} the gravity vector and $\boldsymbol{\gamma}$ the acceleration vector. It is worth noting that gravity and inertia can be neglected in mould components as well as inertia in the solidified regions of the casting.

2.2.1 Mechanical boundary conditions

The boundary $\partial\Omega_1$ of the domain Ω_1 occupied by the part can be divided into two main regions (the extension of contact boundary conditions to the interaction with deformable mould components will be explained in section 2.7):

- $\partial\Omega_{1/mld}$ consists of the boundary regions $\partial\Omega_{1/j}$ of the part facing the mould components (domains $\Omega_j, j \geq 2$). The unilateral contact condition is applied to these surfaces:

$$\begin{cases} \boldsymbol{\sigma} \cdot \mathbf{n} \leq 0 \\ \delta \geq 0 \\ (\boldsymbol{\sigma} \cdot \mathbf{n}) \delta = 0 \end{cases} \quad (4)$$

where δ is the local interface gap width (positive when air gap exists effectively) and \mathbf{n} is the local outward unit normal to the part. The fulfilment of (4) is obtained by means of a penalty condition, which consists in applying a normal stress vector proportional to the normal velocity difference via a penalty constant χ_p (the brackets in the following expression denote the positive part):

$$\mathbf{T} = \boldsymbol{\sigma} \mathbf{n} = -\chi_p \langle (\mathbf{v} - \mathbf{v}_{mld}) \cdot \mathbf{n} \rangle \mathbf{n} \quad (5)$$

The possible tangential friction effects between part and mould are taken into account by a Coulomb friction model. In this case, the previous stress vector has a tangential component, \mathbf{T}_τ , given by:

$$\mathbf{T}_\tau = -\mu_f |\sigma_n| \frac{1}{\|\mathbf{v} - \mathbf{v}_{mld}\|} (\mathbf{v} - \mathbf{v}_{mld}) \quad (6)$$

where σ_n is the normal stress, or contact pressure, and μ_f the friction coefficient.

- $\partial\Omega_{1/pre}$ consists of the regions of $\partial\Omega_1$ not facing the mould, *i.e.* where an external fluid pressure $P_{ext}(t)$ is prescribed. This pressure can be either the atmospheric pressure, on so-called free surfaces, or a prescribed pressure due to the process itself. Consequently, locally, the external stress vector reduces to an applied normal stress vector on $\partial\Omega_{1/pre}$:

$$\mathbf{T} = \boldsymbol{\sigma} \mathbf{n} = -P_{ext}(t) \mathbf{n} \quad (7)$$

2.3 Weak form of mechanical equations

The primitive variables are velocity and pressure. The problem to be solved is then composed of two equations. The first one is the weak form of the momentum equation, also known as the principle of virtual power. Since p is kept as a primitive variable, only the deviatoric part of constitutive equations is accounted for and has to be solved locally in order to determine the deviatoric stress tensor \mathbf{s} . Therefore the second equation consists of the weak form of the volumetric part of the constitutive equations. It expresses the incompressibility of the plastic deformation. This leads to:

$$\begin{cases} \forall \mathbf{v}^* \int_{\Omega} \mathbf{s} : \dot{\boldsymbol{\varepsilon}}^* dV - \int_{\Omega} p \nabla \cdot \mathbf{v}^* dV - \int_{\partial\Omega} \mathbf{T} \cdot \mathbf{v}^* dS - \int_{\Omega} \rho \mathbf{g} \cdot \mathbf{v}^* dV + \int_{\Omega} \rho \gamma \cdot \mathbf{v}^* dV = 0 \\ \forall p^* \int_{\Omega} p^* \text{tr} \dot{\boldsymbol{\varepsilon}}^{vp} dV = 0 \end{cases} \quad (8)$$

The pressure variable appears as a Lagrange multiplier of the plastic incompressibility constraint. The form of the term integrated in the second equation will change according to the local state of the alloy (*i.e.* according to the local temperature). In case of a solid-like constitutive equation (elastic-viscoplastic behaviour), it will be:

$$\text{tr} \dot{\boldsymbol{\varepsilon}}^{vp} = \text{tr} \dot{\boldsymbol{\varepsilon}} - \text{tr} \dot{\boldsymbol{\varepsilon}}^{el} - \text{tr} \dot{\boldsymbol{\varepsilon}}^{th} = \nabla \cdot \mathbf{v} + \frac{3(1-2\nu)}{E} \dot{p} - 3\alpha \dot{T} - \dot{g}_s \Delta \varepsilon^{tr} \quad (9)$$

whereas in case of a liquid-like constitutive equation (pure viscoplastic behaviour), the elastic contribution vanishes, yielding:

$$\text{tr} \dot{\boldsymbol{\varepsilon}}^{vp} = \text{tr} \dot{\boldsymbol{\varepsilon}} - \text{tr} \dot{\boldsymbol{\varepsilon}}^{th} = \nabla \cdot \mathbf{v} - 3\alpha \dot{T} - \dot{g}_s \Delta \varepsilon^{tr} \quad (10)$$

Accordingly, the stress deviator \mathbf{s} in (8a) will result either from a viscoplastic (possibly Newtonian) law, or from an elastic-viscoplastic constitutive equation. In the first case, \mathbf{s} can be easily deduced from (1). Taking the deviatoric part of (1a) and (1b), we have:

$$\mathbf{s} = 2K \left(\sqrt{3} \dot{\boldsymbol{\varepsilon}}_{eq} \right)^{m-1} \text{dev}(\dot{\boldsymbol{\varepsilon}}) \quad (11)$$

which yields the deviatoric stress tensor associated with a given (guessed) velocity field \mathbf{v} , whose corresponding strain rate tensor is $\dot{\boldsymbol{\varepsilon}}$. In the second case (elastic-viscoplastic behaviour), the resolution of (2) is less immediate. A standard return-mapping algorithm (Euler backward implicit scheme) is used, the details of which are given in [18], including existence and uniqueness demonstrations.

2.4 Time discretization

Given the configuration occupied by the cast part at time t , the equations to be solved for $(\mathbf{v}, p)^t$, velocity and pressure field at time t , can be expressed in the following way (for the sake of clarity, we take the case of a thermo-elastic-viscoplastic behaviour in the second equation).

$$\left\{ \begin{array}{l} \forall \mathbf{v}^* \quad \int_{\Omega^t} \mathbf{s}(\mathbf{v}^t) : \dot{\boldsymbol{\varepsilon}}^* dV - \int_{\Omega^t} p^t \nabla \cdot \mathbf{v}^* dV - \int_{\partial\Omega^t} \mathbf{T}^t \cdot \mathbf{v}^* dS - \int_{\Omega^t} \rho \mathbf{g} \cdot \mathbf{v}^* dV + \int_{\Omega^t} \rho \frac{\mathbf{v}^t - \mathbf{v}^{t-\Delta t}}{\Delta t} \cdot \mathbf{v}^* dV = 0 \\ \forall p^* \quad \int_{\Omega^t} p^* (\nabla \cdot \mathbf{v}^t + \frac{3(1-2\nu)}{E} \frac{p^t - p^{t-\Delta t}}{\Delta t} - 3\alpha \dot{T} + \dot{g}_s \Delta \boldsymbol{\varepsilon}^{tr}) dV = 0 \end{array} \right. \quad (12)$$

In this equation, \dot{T} and \dot{g}_s are provided by the thermal resolution. The time derivatives of pressure and velocity are approximated by implicit Euler backward finite difference schemes on the time increment Δt :

$$\dot{p}^t = \frac{1}{\Delta t} (p^t - p^{t-\Delta t}) \quad \gamma^t = \frac{1}{\Delta t} (\mathbf{v}^t - \mathbf{v}^{t-\Delta t}) \quad (13)$$

After resolution, the configuration updating is defined by:

$$\mathbf{x}^{t+\Delta t} = \mathbf{x}^t + \Delta t \mathbf{v}^t + \frac{\Delta t^2}{2} \gamma^t = \mathbf{x}^t + \Delta t \mathbf{v}_{mat} \quad \text{with} \quad \mathbf{v}_{mat} = \frac{3}{2} \mathbf{v}^t - \frac{1}{2} \mathbf{v}^{t-\Delta t} \quad (14)$$

Except for mould filling analysis, the material velocities and their time derivative remain rather low. Therefore the second order acceleration terms in (14) may be neglected. In this case, $\mathbf{v}_{mat} = \mathbf{v}^t$.

2.5 Finite element discretization and resolution

In the codes THERCAST[®] and R2SOL, the finite element mesh is composed of linear tetrahedra and triangles, respectively. The P1+/P1 mini-element, initially proposed by Arnold *et al* [19] and Fortin and Fortin [20], is used. In an element, the velocity field is mainly linear continuous, but includes a central correction of “bubble”-type in order to satisfy the Brezzi-Babuska condition. This velocity correction varies linearly on each of the four sub-tetrahedra in 3D (respectively, three sub-triangles in 2D), between its value at the centre of the element and zero on all the facets (resp., edges) of the element [17]. The momentum equation is then projected onto the P1 space and onto the “bubble” space [15-17]. Using the condensation of the bubble degrees of freedom (which are internal to the element) during the finite element assembly process, this leads to the resolution of a non linear equation whose unknowns are the vector \mathbf{V} of nodal velocities, and the vector \mathbf{P} of nodal pressures:

$$\mathbf{R}_{mech}(\mathbf{V}, \mathbf{P}) = 0 \quad (15)$$

This set of equations is solved by a Newton-Raphson method. At each Newton-Raphson iteration, the resolution of the set of linearized equations for (\mathbf{V}, \mathbf{P}) is performed by a preconditioned iterative solver.

2.6 Concurrent treatment of solid and liquid regions

Such a mini-element formulation provides a perfect compatibility between the treatment of an elastic-viscoplastic medium and a pure viscoplastic or Newtonian medium. Therefore, it allows to treat simultaneously the solidified zones and the liquid or mushy pools of a casting. The unified form of the mechanical equations can be written in the following way:

$$\begin{cases} \forall \mathbf{v}^* & \int_{\Omega} \left\{ \begin{matrix} \mathbf{s}^{evp} \\ \mathbf{s}^{vp} \end{matrix} \right\} : \dot{\boldsymbol{\varepsilon}}^* dV - \int_{\Omega} p \nabla \cdot \mathbf{v}^* dV - \int_{\partial\Omega} \mathbf{T} \cdot \mathbf{v}^* dS - \int_{\Omega} \rho \mathbf{g} \cdot \mathbf{v}^* dV + \int_{\Omega} \rho \boldsymbol{\gamma} \cdot \mathbf{v}^* dV = 0 \\ \forall p^* & \int_{\Omega} p^* \left(\nabla \cdot \mathbf{v} + \begin{cases} 3\dot{p}(1-2\nu)/E \\ 0 \end{cases} - 3\alpha\dot{T} - \dot{g}_s \Delta \boldsymbol{\varepsilon}^{tr} \right) dV = 0 \end{cases} \quad (16)$$

The braces in both equations allow the distinction between the two constitutive models. This choice is done when assembling each finite element, depending on the temperature at its centre. If the temperature exceeds the critical temperature T_C , then the whole element is considered viscoplastic (lower line in braces), otherwise it is elastic-viscoplastic (upper line in braces).

2.7 Mechanical coupling algorithm for part-mould and mould-mould interactions

The objective is to model mould deformation and contact interactions occurring either between the cast part and the mould components or between the mould components themselves. This problem of contact between several deformable bodies is modelled by means of the penalty approach.

In practice, along an interface between two domains Ω_i and Ω_j , we choose arbitrarily to penalize the penetration of Ω_i into Ω_j , which means that in the resolution of the mechanical equilibrium of Ω_i , the following penalty term is added:

$$\int_{\partial\Omega_{i/j}} -\chi_p \left\langle (\mathbf{v} - \mathbf{v}^{(j)}) \cdot \mathbf{n} \right\rangle \mathbf{n} \cdot \mathbf{v}^* dS \quad (17)$$

where $\mathbf{v}^{(j)}$ is the respective local velocity of the domain Ω_j , \mathbf{n} being the normal at interface and χ_p the penalty coefficient. Accordingly, considering the action-reaction principle, the following normal stress vector \mathbf{T} is applied to the surface of Ω_j :

$$\mathbf{T} = -\chi_p \left\langle (\mathbf{v}^{(j)} - \mathbf{v}^{(i)}) \cdot \mathbf{n} \right\rangle \mathbf{n} \quad (18)$$

During the simulation of a solidification process, the equilibrium of each domain with respect to its neighbouring domains is computed. Since the cooling is generally not very rapid, there is no need to solve simultaneously the equilibrium of all bodies (this would be obtained by a heavy and costly fix point procedure or by a global computation including all domains). A staggered scheme is preferred, each domain being calculated only once per increment.

3. Heat transfer

In THERCAST[®] software, the heat transfer problem is solved on the different subdomains Ω_i involved in a solidification problem, *i.e.* the solidifying part and the different constitutive components of the casting mold. In this paper, it is chosen not to describe the multidomain resolution, see [15]. The heat transfer equation, to be solved on of the subdomains Ω_i of the casting problem, possibly including phase change – in the part – but without any internal heat source, can be written:

$$\rho \frac{dH}{dt} = \nabla \cdot (\lambda \nabla T) \quad (19)$$

where the specific enthalpy H is defined by:

$$H = \int_{T_0}^T c_p(\tau) d\tau + (1 - g_s) L \quad (20)$$

with T_0 an arbitrary reference temperature, c_p the specific heat and L the specific latent heat of fusion. In the present study, the solidification path $g_s(T)$ is considered given. Therefore, the value of the enthalpy can be calculated for any value of the temperature.

The following conditions on the boundary $\partial\Omega_i$ of the subdomain Ω_i are considered:

- Prescribed outward heat flux:

$$-\lambda \nabla T \cdot \mathbf{n} = \phi_{imp} \quad (21)$$

where \mathbf{n} denotes the outward normal unit vector and λ the thermal conductivity.

- Convection:

$$-\lambda \nabla T \cdot \mathbf{n} = h_c (T - T_{ext}) \quad (22)$$

where T_{ext} denotes the external temperature and h_c the convection coefficient.

- Radiation:

$$-\lambda \nabla T \cdot \mathbf{n} = \varepsilon_r \sigma_r (T^4 - T_{ext}^4) \quad (23)$$

where ε_r is the emissivity of the material (considered as a grey body), σ_r the Stefan-Boltzmann constant. It is to be noticed that equation (23) can be cast in the same form as equation (22) by linearization. It is then possible to express a mixed convection-radiation boundary condition:

$$-\lambda \nabla T \cdot \mathbf{n} = h_{cr} (T - T_{ext}) \quad (24)$$

with

$$h_{cr} = h_c + \varepsilon_r \sigma_r (T^2 + T_{ext}^2)(T + T_{ext}) \quad (25)$$

- Prescribed temperature:

$$T = T_{imp} \quad (26)$$

- Exchange with another subdomain Ω_j :

$$-\lambda \nabla T \cdot \mathbf{n} = h_{ij} (T - T_j^{surf}) \quad (27)$$

where h_{ij} is the heat transfer coefficient of the interface between Ω_i and the facing subdomain Ω_j , whose surface temperature is T_j^{surf} .

The standard Galerkin finite element discretization leads to the classical set of non linear equations:

$$\mathbf{M}\dot{\mathbf{H}} + \mathbf{K}\mathbf{T} = \mathbf{Q} \quad (28)$$

with \mathbf{M} the mass matrix, \mathbf{K} the conduction matrix, \mathbf{Q} the right hand side vector, $\dot{\mathbf{H}}$ the vector of enthalpy rates at nodes and \mathbf{T} the vector of nodal temperatures.

The phase change affecting the part is treated using the technique proposed by Lemmon [21]. Applying this technique to linear simplex elements (P1 tetrahedra), an element-wise constant value of the effective heat capacity is approximated by the following regularization formula:

$$c_{eff} = \frac{\partial H}{\partial T} \approx \frac{\|\nabla H(T)\|}{\|\nabla T\|} \quad (29)$$

The set of equations (28) then becomes:

$$\mathbf{C}\dot{\mathbf{T}} + \mathbf{K}\mathbf{T} = \mathbf{Q} \quad (30)$$

with $\dot{\mathbf{T}}$ the vector of nodal temperature rates, \mathbf{C} the heat capacity matrix. This latter matrix is then temperature dependent within the solidification interval (and possibly outside, due to c_p variations). In addition, matrix \mathbf{K} and vector \mathbf{Q} may depend on temperature.

A Euler backward implicit scheme is used for the time discretization of this equation, which leads to a set of non linear equations to be solved for the values of the temperatures at finite element nodes at the end of the time increment considered:

$$\mathbf{R}_{therm}(\mathbf{T}^{t+\Delta t}) = 0 \quad (31)$$

A Newton-Raphson scheme is used to solve it.

4. Solute conservation

4.1 On the modeling of the mushy region

The modelling of macrosegregation requires a refinement of the previous mechanical model in order to account for the liquid flow in the mushy region, which is known to have a major influence in the redistribution of solute in the whole domain. Such a flow is usually assimilated to that of a fluid through a porous medium governed by the Darcy's law. Adopting the same

assumptions of most macrosegregation models, *i.e.* Newtonian flow and rigid and fixed solid phase, the momentum equation (3) in this region takes the form [22-23]

$$\nabla \cdot (\mu \nabla \mathbf{v}) - \nabla p + \rho \mathbf{g} - \frac{\mu}{K} \mathbf{v} - \rho \frac{d\mathbf{v}}{dt} = 0 \quad (32)$$

resembling the Navier-Stokes equation governing the flow in the fully liquid region, supplemented by the fourth term defining the drag force arising from the Darcy's law. Now, \mathbf{v} is defined as the average mixture velocity. The permeability of the solid skeleton is defined by the well-known Carman-Kozeny formula

$$K = \frac{\lambda_2^2 g_l^3}{180(1 - g_l)^2} \quad (33)$$

Another important feature of equation (32) concerns the density ρ , which is assumed to have a constant value $\rho_0 = \rho(T_0, w_0^l)$, except in the gravity term, where it varies according to the Boussinesq's approximation

$$\rho = \rho_0 [1 - 3\alpha(T - T_0) - \beta_c(w^l - w_0^l)] \quad (34)$$

in order to model natural convection induced by thermal and solutal gradients.

Regarding the thermal field, equation (19) remains valid in the mushy region.

4.2 Macrosegregation in binary alloys

Let us assume a binary alloy where segregation at the microscopic scale obeys the lever rule. We have:

$$w^s = kw^l \quad (35)$$

with w^s and w^l being the mass concentration in the solid and liquid phase, both assumed homogeneous. Considering all the assumptions of this section, the macroscopic solute conservation equation takes the form [24]:

$$\frac{\partial w}{\partial t} + \mathbf{v} \cdot \nabla w^l - \nabla \cdot (\varepsilon \nabla w) = 0 \quad (36)$$

Although solute diffusion is usually negligible in metallic alloys, the solute diffusivity ε is assumed to have a positive value (even very small) in order to improve numerical stability.

In THERCAST[®], equation (36) was first solved in Eulerian coordinates using the Streamline Upwind Petrov-Galerkin (SUPG) formulation [25]. In this work, following Kämpfer [26], we use a splitting scheme applied to the advection term:

$$\nabla w^l \approx \nabla w - \nabla w^0 + \nabla w^{l0} \quad (37)$$

where the superscript 0 refers to known values of the variables at the previous time step. Invoking (37), equation (36) can be rewritten using the particle (total) derivative of w :

$$\frac{dw}{dt} - \nabla \cdot (\epsilon \nabla w) = Q^0 \quad (38)$$

where

$$Q^0 = \mathbf{v} \cdot \nabla (w^0 - w'^0) \quad (39)$$

In such a way, the solute conservation equation becomes self-adjoint (*i.e.*, system matrix is symmetric) and can be solved by in the same way as the energy equation.

5. ALE formulation

The ALE method has been implemented according to a staggered scheme at each time increment. In a first step the material velocities are calculated by solving (15). In a second step, the mesh velocities, denoted \mathbf{v}_{msh} , are calculated, which allows us to update the domain occupied by the cast alloy. In the context of solidification, there are three main problems to address:

- the computation of the mesh velocity field;
- the accounting for the velocity difference $\mathbf{v}_{mat} - \mathbf{v}_{msh}$ in energy, solute and momentum equations;
- the determination of the areas of the computational domain that should be treated as Lagrangian and Eulerian-Lagrangian.

Those three different topics are presented in the next sections.

5.1 Mesh updating

According to (14) and neglecting second order terms, a Lagrangian-type mesh updating scheme would be defined by:

$$\mathbf{X}^{t+\Delta t} = \mathbf{X}^t + \Delta t \mathbf{V}^t \quad (40)$$

where \mathbf{X} denotes the global vector of nodal coordinates.

In ALE formulation, the displacement of the nodes generally differs from the displacement of the material particles. For a time increment, we can write the following equation relating the updated position of nodes and the mesh velocity:

$$\mathbf{X}^{t+\Delta t} = \mathbf{X}^t + \Delta t \mathbf{V}_{msh} \quad (41)$$

where \mathbf{V}_{msh} denotes the global vector of mesh velocities at nodes.

Consequently and from a general point of view, the determination of \mathbf{v}_{msh} can be guided by various considerations: geometrical regularization of the mesh, in order to control the shape factors of the elements, change of mesh density in certain regions, in order to approach objective local mesh sizes provided by other criteria, such as error estimation. In this latter case, the mesh motion can result from combined regularization and adaptivity. In the sequel, we will restrict our

presentation to geometrical regularization. We will distinguish the treatment of internal nodes and of boundary nodes, for which additional constraints on volume conservation apply.

5.1.1 Regularization of interior nodes

The nodal velocities are calculated in order to minimise the distortion of the updated mesh. This can be achieved by writing that, after updating, each interior node n should be as close as possible to the centre of gravity of the polygon joining its neighbouring nodes. Denoting $\tau_{nb}(n)$ the set of nodes connected to node n , and $nb(n)$ its cardinal, the problem to be solved can be expressed as follows:

Find the nodal field V_{msh} such that :

$$\text{Min}_{V_{msh}} \sum_n \left\| X^{n,t} + \Delta t V_{msh}^n - \frac{1}{nb(n)} \sum_{m \in \tau_{nb}(n)} (X^{m,t} + \Delta t V_{msh}^m) \right\|^2 \quad (42)$$

This problem is solved by an iterative procedure of Jacobi type. At each iteration ν and for each interior node n , the new estimate of the nodal mesh velocity is calculated in the following way:

$$V_{msh}^{n(\nu+1)} = \frac{1}{\Delta t} \left[\frac{1}{nb(n)} \sum_{m \in \tau_{nb}(n)} (X^{m,t} + \Delta t V_{msh}^{m(\nu)}) - X^{n,t} \right] \quad (43)$$

5.1.2 Regularization of boundary nodes, constraint on volume conservation

An equivalent expression can be derived for boundary nodes, but the summation in (42) and (43) should be reduced to the set of neighbouring nodes located on the domain boundary. Moreover, as said previously, an additional constraint on volume conservation must be fulfilled simultaneously. The flow rate of both the material velocity field and the mesh velocity field through the mesh boundary must be equal:

$$\mathbf{v}_{msh} \cdot \mathbf{n} = \mathbf{v}_{mat} \cdot \mathbf{n} \quad (44)$$

with \mathbf{n} the outward unit normal. In order to ensure that equation (44) correctly expresses material flux conservation, we use in this relation the so-called “consistent” normal vectors defined at boundary nodes, as suggested by Gray [27] and Engelman *et al* [28]. Those vectors are such that any tangential nodal velocity (*i.e.* a velocity which is orthogonal to the consistent normal vector) provides a null contribution to the flux through the discretized surface. In 3D, in the case of linear elements, the consistent¹ normal vector at each surface node m is defined by the average of the normals of the surrounding facets weighted by their surface:

¹ According to their definition, these normal vectors should rather be named “conservative” normals.

$$\tilde{\mathbf{n}}^m = \frac{1}{\left\| \sum_{f \in \tau(m)} S^f \mathbf{n}^f \right\|} \sum_{f \in \tau(m)} S^f \mathbf{n}^f \quad (45)$$

where $\tau(m)$ denotes the set of triangular facets f the surface node m belongs to, S^f being the area of each facet. The demonstration of (45) has been first proposed by Bellet [29] and is given in appendix of the present paper. In 2D, the same expression holds, S^f denoting the length of the boundary edges the node m belongs to.

The fulfilment of the condition (44) is forced by a penalty technique which is applied locally. Given a boundary node q , we denote $\tau_{nb/s}(q)$ the set of boundary nodes connected to node q , of cardinal $nb/s(q)$. At iteration ν , the new estimate of the velocity field of the node is defined by:

$$\mathbf{V}_{msh}^{q(\nu+1)} = \arg\min_{\mathbf{V}_{msh}^q} \left\{ \left\| \mathbf{X}^{q,t} + \Delta t \mathbf{V}_{msh}^q - \frac{1}{nb/s(q)} \sum_{m \in \tau_{nb/s}(q)} (\mathbf{X}^{m,t} + \Delta t \mathbf{V}_{msh}^{m(\nu)}) \right\|^2 + \frac{\chi}{2} (\mathbf{V}_{msh}^q - \mathbf{V}_{mat}^q) \cdot \tilde{\mathbf{n}}^q \right\} \quad (46)$$

where the penalty factor χ is a large penalty constant. The new estimate $\mathbf{V}_{msh}^{q(\nu+1)}$ is easily obtained as the solution of a set of linear equations.

In three dimensions, the difficulty of the procedure lies essentially on the treatment of nodes which are in the vicinity of sharp edges and corners of moulds and/or belong to symmetry planes. In this case, the local penalty method can be applied to enforce (44) for several normal vectors.

The iterative procedure is repeated up to stagnation (*i.e.* minor relative corrections of the nodal velocities) and the following updating scheme of nodes is then applied:

$$\mathbf{X}^{t+\Delta t} = \mathbf{X}^t + \Delta t \mathbf{V}_{msh}^{(\infty)} \quad (47)$$

5.2 Treatment of advection terms

Knowing the mesh velocity, it is now necessary to proceed to the updating of nodal fields. Consider first the temperature field T . Its updating is done by writing for each node:

$$T^{t+\Delta t} = T^t + \frac{\partial_m T}{\partial t} \Delta t \quad (48)$$

where $\partial_m T / \partial t$ denotes the time derivative of T with respect to the mesh (the rate of variation of temperature at a given point of the mesh) which is related to the material derivative by the following expression:

$$\frac{dT}{dt} = \frac{\partial_m T}{\partial t} + (\mathbf{v}_{mat} - \mathbf{v}_{msh}) \cdot \nabla T \quad (49)$$

In the literature, this expression is frequently directly implemented in the weak form of the heat transfer equation. Streamline Upwind - Petrov-Galerkin (SUPG) techniques are then used,

stabilising the advective terms by use of artificial diffusion along streamlines [25]. Here we proceed in a different way, as initially suggested by Chenot and Bellet [30]. Once the heat transfer problem has been solved on the time increment, the total (material) time derivative of the temperature is known at each node. After computation of \mathbf{v}_{mat} and \mathbf{v}_{msh} , the updating of the temperature field can be obtained by writing (48-49) at each node, yielding:

$$\begin{aligned} T^{t+\Delta t} &= T^t + \Delta t \left(\frac{T_{Lag}^{t+\Delta t} - T^t}{\Delta t} - (\mathbf{v}_{mat} - \mathbf{v}_{msh}) \cdot \nabla T \right) \\ &= T_{Lag}^{t+\Delta t} - \Delta t (\mathbf{v}_{mat} - \mathbf{v}_{msh}) \cdot \nabla T \end{aligned} \quad (50)$$

where $T_{Lag}^{t+\Delta t}$ denotes the temperature at the Lagrangian update of the node considered. Referring to figure 2, this expression appears as a first order spatial development of the temperature field around the location $\mathbf{x}_{Lag}^{t+\Delta t}$. The determination of the new temperature $T^{t+\Delta t}$ of the node only requires the nodal temperature gradient. Using an upwind technique, this nodal gradient is computed in the upstream element, according to the advection velocity $\mathbf{v}_{mat} - \mathbf{v}_{msh}$.

In case of macrosegregation analysis, the average solute concentration w is transported exactly in the same way.

In order to express the acceleration terms in the momentum equation, a transport of the material velocity field is necessary. In (12-13), the velocity $\mathbf{v}^{t-\Delta t}$ is the material velocity of the particle at the previous time level. Hence, after configuration updating, this requires a pure transport of the velocity field. This is achieved by a similar scheme as (48-49), but in which the material derivative is taken equal to zero:

$$\mathbf{v}^t(\mathbf{x}^{t+\Delta t}) = \mathbf{v}^t(\mathbf{x}^t) - [\nabla \mathbf{v}^t(\mathbf{x}^t)](\mathbf{v}_{mat}(\mathbf{x}^t) - \mathbf{v}_{msh})\Delta t \quad (51)$$

Referring to figure 2, it can be seen once again that (51) is nothing but a first order spatial development of the material velocity field in the upstream element associated with the nodal position \mathbf{x}^t .

It should be noted that the calculation of $\mathbf{v}^t(\mathbf{x}^{t+\Delta t})$ could be achieved using, for instance, the method of characteristics, as suggested by Pironneau [31]. In the two-dimensional mould filling computations presented in the present paper, an approximating method has been adopted, sometimes named "pseudo Lagrangian" (fig. 3). In this method, an auxiliary Lagrangian update $\Omega_{Lag}^{t+\Delta t}$ of the configuration is used. It is defined by (14) or (40). Considering the position $\mathbf{x}^{t+\Delta t}$, the associated element e of $\Omega_{Lag}^{t+\Delta t}$ and the local coordinates (ξ, η) in this element are determined. Therefore, $\Omega_{Lag}^{t+\Delta t}$ being a material update of Ω^t , the value $\mathbf{v}^t(\mathbf{x}^{t+\Delta t})$ is computed by direct interpolation in element e of Ω^t :

$$\mathbf{v}^t(\mathbf{x}^{t+\Delta t}) = N_n(\xi, \eta) \mathbf{V}^{n,t} \quad (52)$$

where N_n denotes the interpolation function attached to node n .

5.3 On the accuracy of the transport scheme

The update of any variable as described above has proved to be accurate only if Δt remains small enough, such that

$$\Delta t \leq \Delta t_{\max} = \text{Max}_m \frac{h^e}{|V_{mat}^m - V_{msh}^m|} \quad (53)$$

being h^e the distance from the node m to the opposite side along the direction of $V_{mat}^m - V_{msh}^m$, across the upwind element.

In THERCAST[®], following Jaouen [15], this restriction is circumvented by carrying out the transport during $[t, t+\Delta t]$ in n sub-steps $[t, t_1]$, $[t_1, t_2], \dots, [t_{n-1}, t+\Delta t]$, being $t_i = t + i\Delta t_{\max}$. In practice, n should not exceed 6 in order to keep a satisfactory accuracy, a condition that is easily satisfied in typical casting simulations.

This strategy has been validated by means of the well-known benchmark problem of De Vahl Davis and Jones [32-33] dealing with the natural convection of a Boussinesq fluid contained in a square cavity. A 1 m²-domain is modelled in 3D assuming a thin layer where the wide faces are adiabatic. It is spatially discretized using an unstructured, fixed, tetrahedral finite element mesh is used, with a uniform element size of 2.6 cm. Time step is constant and equal to 0.25 s. Some significant results for the case of Prandtl number equal to 0.71, and two different Raleigh numbers are shown in Table 1. While condition (53) is satisfied a priori for $Ra=10^3$ ($\Delta t/\Delta t_{\max}=0.63$), four substeps were taken ($\Delta t/\Delta t_{\max}=3.38$) in case $Ra=10^4$, preserving a proper accuracy.

5.4 Lagrangian and Eulerian-Lagrangian zones

Regarding now the global treatment of a casting, the idea consists in defining the solidified regions as Lagrangian (convected mesh) and the liquid or mushy ones as Eulerian-Lagrangian (regularized mesh under the constraint (44)). Therefore each node is affected by one of the two formulations, according to the following rule, as illustrated in figure 4.

- ✓ Each node belonging to at least one solid-like element (*i.e.* an element whose constitutive equation has been chosen elastic-viscoplastic, see section 2.6) is treated as Lagrangian: its mesh velocity equals its material velocity.
- ✓ All other nodes, which therefore belong to liquid-like elements only, are treated as Eulerian-Lagrangian: their mesh velocity is calculated as described in section 5.1.

This ALE formulation prevents the mesh from degenerating when fluid motion occurs in the casting, due to thermal convection. Also it allows the mesh boundary to follow the evolution of the free surface of the remaining liquid pool and then to model pipe formation.

5.5 Synthetic ALE algorithm

To conclude this section, the chain of the major steps of the developed ALE algorithm is given in box 1.

$\mathbf{x}^t, \mathbf{v}^{t-\Delta t}, p^{t-\Delta t}, T^t, w^t$: variables known at the beginning of a new time increment	
1) Resolution of energy conservation (31)	$T_{Lag}^{t+\Delta t}$
2) Resolution of solute conservation (38)	$w_{Lag}^{t+\Delta t}$
3) Resolution of momentum conservation (15)	\mathbf{v}^t, p^t
4) Lagrangian updating of configuration (14) or (40) (only if direct interpolation is used in step 7)	$\mathbf{x}_{Lag}^{t+\Delta t}$
5) Calculation of mesh velocity field (43) and (46)	\mathbf{v}_{msh}
6) Updating of configuration (47)	$\mathbf{x}^{t+\Delta t}$
7) Transport for particle derivatives, by nodal upwind (50-51) or by direct interpolation (52)	$T^{t+\Delta t}, w^{t+\Delta t}, \mathbf{v}^t(\mathbf{x}^{t+\Delta t})$
8) Updating of variables	
$t \leftarrow t + \Delta t, \mathbf{x}^t \leftarrow \mathbf{x}^{t+\Delta t}, \mathbf{v}^{t-\Delta t} \leftarrow \mathbf{v}^t, p^{t-\Delta t} \leftarrow p^t, T^t \leftarrow T^{t+\Delta t}, w^t \leftarrow w^{t+\Delta t}$	

Box 1: ALE algorithm. Summary of the main procedures carried out during a time increment.

6. Applications

6.1 Two-dimensional modelling of mould filling

We briefly present here the results already detailed in [14]. Two-dimensional calculations performed with the code R2SOL have been compared to experimental results obtained with a water model, in which the experimental flow can be easily observed through a transparent mould made of plexiglas[®] with a numerical video recorder. The experimental device is shown on figure 5. The square cavity is 320 mm high and its thickness is 20 mm.

The simulation has been carried out using the 6-node quadratic element P2+/P1 available at that time in R2SOL, the mechanical solver being of Uzawa type. Also the statistic turbulence model $k-\varepsilon$ was used because of high velocities in the runner, the nominal Reynolds number being about 20000 (for further details on these points, see [14, 34]).

Figure 6 shows a typical comparison between the computed and observed evolution of the free surface. Taking into account the fact that some characteristics of the experimental flow can be attributed to three-dimensional effects, such as wetting of the jet on lateral walls for instance, the agreement is very good.

6.2 A pure Eulerian calculation: macrosegregation in a square cavity

Let us consider a square cavity of $10 \times 10 \text{ cm}^2$ area, full of 0.2%wt-C steel, initially liquid at 1523°C . The cavity is cooled by convection to the environment through the vertical walls. Invoking symmetry conditions, just a half of the cavity is modelled. Mechanical and thermal boundary conditions are shown in figure 7. Material data and other execution parameters are listed in table 2. For the 3D analysis using THERCAST[®], a 1 mm-thick slice delimited by adiabatic walls is considered. The mesh used for the analysis, composed of 8911 linear tetrahedral elements (3112 nodes), is shown on the right of figure 7. Regarding time integration, a constant time step of 0.1 s has been used. Results are compared to those of the 2D finite volume code SOLID, developed by Combeau *et al* [35] and already validated, using the same time step and a structured uniform mesh.

Macrosegregation patterns in the cavity once it is totally solidified ($t = 1000 \text{ s}$) are plotted in figure 8. Both SOLID and THERCAST[®] solution are in good agreement. The extreme values of positive and negative segregation (*i.e.*, $w > 0.2 \%$ and $w < 0.2 \%$, respectively) predicted by THERCAST[®] are higher than those of SOLID. Let us note that similar differences between SOLID finite-volume approach and a 2D finite-element code have been previously reported by Ahmad *et al* [36].

6.3 Three-dimensional modelling of the solidification of a large casting

The part studied here is an element of very large electro-magnets: each magnet is composed of two identical parts, whose shape is illustrated in figure 9. These parts are very specific by their weight (125 tons each), their dimensions ($2.5 \times 7.0 \times 1.0 \text{ m}$) and the steel grade (carbon-free steel, whose chemical composition is close to pure iron). They are cast in sand moulds.

A full thermomechanical computation has been done in order to precisely determine the shape of the primary shrinkage defect in the riser. Using symmetry conditions, only half of the casting has been calculated. As shown in figure 9, the configuration includes seven subdomains: the cast part and six components of the mould. The part has approximately 120 000 tetrahedral elements and the mould subdomains 373 000. In a first approach, only the deformations affecting the part have been calculated. The part cools down in the mould during approximately 127 h. Then the mould is removed, which is associated in the simulation with a global change of the thermomechanical boundary conditions. The same heat transfer coefficient is then applied to the entire surface of the part, to model heat transfer with surrounding air by convection, except on the lower surface which is in contact with the basement of the mould. The heat exchange through this interface is defined by a higher heat exchange coefficient. The complete cooling of the part has been simulated, until a maximum temperature of about 50°C has been reached.

In figure 10, the shape of the pipe is shown for process times 2, 8, 16 and 32 h. The last region to solidify (after 36 h) is located at the bottom of the v-shape of the pipe shrinkage, which has almost reached its final shape at this time. This figure illustrates well the capacity of ALE formulation. The mesh follows the evolution of the free surface of the alloy because of the flux condition (44), while the free surface remains perfectly horizontal, which is a consequence of the

clear distinction between liquid-type and solid-type constitutive equations. In the other regions, the mesh is regularized. Twenty complete remeshings have been needed in order to avoid mesh degeneracy along the pipe surface.

The final shape of the pipe calculated by the simulation is given in figure 11a. There is a reasonably good agreement with the v-shape experimentally measured (fig. 11b). The predicted maximum depth is 1.48 m, versus 1.43 m measured, which is excellent. However the precise shape of the pipe is not obtained, and complementary studies are needed, especially regarding the sensibility of the results to the mesh size, and to the material parameters: transition temperature between liquid and solid-type constitutive equations, values of rheological parameters.

6.4 An example of simulation combining solid deformation and liquid convection

The solidification of a 3.3 tons steel ingot is studied. The axisymmetric geometry is shown in figure 12 and the simulation has been carried out with the two-dimensional software R2SOL. The configuration includes five subdomains: the cast ingot, (height 1.830 m, maximum radius 0.331 m) and four mould components. The part has approximately 4800 triangular elements (mesh size range: 2.5 mm – 30 mm). In a first approach, the mould has been considered as non deformable. A thermomechanical simulation of the solidification and cooling down process has been carried out. The advancement of the solidification process is illustrated by figure 12, in which the concurrent fluid flow, due to thermal convection, and solid deformation, due to solidification and thermal shrinkage can be seen. The change in the free surface level can be seen, as well as the formation of air gaps between the ingot and the mould components. In figure 13, details are given in the top region of the ingot. The formation of vertical and radial air gaps is shown. Regarding free surface, it can be seen on figure 13c that it is almost flat, because of an efficient thermal protection which minimizes the thermal gradients in the riser. The gap formation phenomena affecting the bottom of the ingot are shown in figure 14. In this figure, the solid-type elements have been coloured in order to illustrate the ALE strategies described in sections 2 and 5.

7. Conclusion

The proposed ALE method is based upon regularization algorithms, in order to determine the appropriate mesh velocity for both interior and boundary nodes. Special attention has been paid to free surface evolution, for which the use of conservative normal vectors permits mass conservation. The regularization algorithms are associated with a nodal upwind technique for the discretization of advection terms in the conservation equations. In this paper, we have illustrated the application of this ALE method to mould filling, solute transport and thermomechanical calculations.

- In mould filling two-dimensional simulations, it has been shown that the proposed ALE method offers a significant advantage regarding the determination of the motion of free surfaces, by comparison with more classical Eulerian finite element methods, based on fixed meshes and VOF formulations. However, the three-dimensional extension of such a technique is not straightforward, especially because of the tremendous complexity of the three-dimensional remeshing procedures that would be needed in the zones of flow

merging. In the authors' opinion, a future three-dimensional extension should rather be based upon the combination of mesh regularization and VOF formulation, which should lead to significant improvements in front tracking, in comparison with existing Eulerian codes.

- In solidification analysis, the essential merit of the proposed method is to make possible a concurrent analysis of the deformation of solidified zones and of the fluid flow present in liquid regions. Therefore, it is now possible in a single numerical simulation to account for complex physical phenomena that can be possibly coupled, such as air gap formation associated with part distortion, heat transfer, thermal convection and free surface evolution. In a near future, the coupling of mesh regularization with mesh adaptivity, in order to refine the mushy zone, will increase the accuracy of macrosegregation and thermomechanical calculations.

Acknowledgement

This work has been supported by the French Ministry of Industry, the French Technical Centre of Casting Industries (CTIF) and the companies Arcelor-Irsid, Ascometal, Atlantic Industrie, Aubert et Duval, Erasteel, Industeel and PSA.

V.D. Fachinotti is also granted by the Argentine Scientific and Technical Research Council (CONICET).

References

- [1] A. Bourg, A. Latrobe, P. Laty, G. Kreziak and C. Rigaut, Predicting the mold filling time with Simulor, Proc. NUMIFORM'92 Int. Conf. on Numerical Modelling of Forming Processes, J.L. Chenot, R.D. Wood and O.C. Zienkiewicz (eds.), Balkema, Rotterdam (1992) 777-785.
- [2] M. Barkhudarov, H. You, J. Ortega, J. Beech, S.B. Chin and D.H. Kirkwood, Experimental validation and development of Flow-3D for casting problems, Proc. 6th Int. Conf. on Modelling of Casting, Welding and Advanced Solidification Processes, The Minerals Metals and Materials Society, Warrendale, Pennsylvania (1993) 421-434.
- [3] D.M. Waite and M.T. Samonds, Finite element free surface modeling, Proc. 6th Int. Conf. on Modeling of Casting, Welding and Advanced Solidification Processes, T.S. Piwonka, V. Voller and L. Katgerman (eds.), The Minerals Metals and Materials Society (1993) 357-364.
- [4] R. Codina, U. Schäfer and E. Oñate, Mold filling simulation using finite elements, Int. J. Num. Meth. Heat Fluid Flow 4 (1994) 291-310.
- [5] R.W. Lewis, A.S. Usmani and J.T. Cross, Efficient mold filling simulation in castings by an explicit finite element method, Int. J. Num. Meth. Fluids 20 (1995) 493-506.
- [6] F. Mampaey and Z.A. Xu, Simulation and experimental validation of mold filling, Proc. 7th Int. Conf. on Modeling of Casting, Welding and Advanced Solidification Processes, M. Cross and J. Campbell (eds.), The Minerals Metals and Materials Society (1995) 3-14.
- [7] J.D. Zhu and I. Ohnaka, Computer simulation of fluid flow and heat transfer in partially reinforced casting, Proc. 7th Int. Conf. on Modeling of Casting, Welding and Advanced Solidification Processes, M. Cross and J. Campbell (eds.), The Minerals Metals and Materials Society (1995) 23-30.
- [8] M. Médale and M. Jaeger, Numerical simulation of incompressible flows with moving interfaces, Int. J. Num. Meth. Fluids 24 (1997) 615-638.
- [9] Magmasoft, <http://www.magmasoft.com> (2003).
- [10] Procast, <http://www.calcom.ch/Products/Procast.html>, <http://www.ues-software.com/subhtm/products/procast.htm> (2003).
- [11] C.W. Hirt and B.D. Nichols, Volume of fluid (vof) method for the dynamics of free boundaries, J. Comp. Phys. 39 (1981) 201-225.
- [12] S.E. Navti, K. Ravindran, C. Taylor and R.W. Lewis, Finite element modelling of surface tension effects using a Lagrangian-Eulerian kinematic description, Comput. Meth. Appl. Mech. Engrg. 147 (1997) 41-60.
- [13] R.W. Lewis, S.E. Navti and C. Taylor, A mixed Lagrangian-Eulerian approach to modelling fluid flow during mold filling, Int. J. Num. Meth. Fluids 25 (1997) 931-952.
- [14] L. Gaston, A. Kamara and M. Bellet, An Arbitrary Lagrangian-Eulerian finite element approach to non-steady state turbulent fluid flow with application to mold filling in Casting, Int. J. Num. Meth. Fluids 34 (2000) 341-369.
- [15] O. Jaouen, Modélisation tridimensionnelle par éléments finis pour l'analyse thermomécanique du refroidissement des pièces coulées (Three-dimensional finite element modelling for the

thermomechanical analysis of the cooling of castings), Ph.D. Thesis (in french), Ecole des Mines de Paris (1998).

[16] M. Bellet and O. Jaouen, Finite element approach of thermomechanics of solidification processes, Proc. Int. Conf. On Cutting Edge of Computer Simulation of Solidification and Casting, Osaka, I. Ohnaka and H. Yasuda (eds.), The Iron and Steel Institute of Japan (1999) 173-190.

[17] M. Bellet, O. Jaouen and I. Poitault, An ALE-FEM Approach to the thermomechanics of solidification processes with application to the prediction of pipe shrinkage, to be published in Int. J. Num. Meth. for Heat & Fluid Flow (2003).

[18] M. Bellet, F. Decultieux, M. Ménaï, F. Bay, C. Levailant, J.L. Chenot, P. Schmidt, I.L. Svensson, Thermomechanics of the cooling stage in casting processes: 3D finite element analysis and experimental validation, Metall. and Mat. Trans. 27B (1996) 81 - 99.

[19] D.N. Arnold, F. Brezzi and M. Fortin, A stable finite element for Stokes equation, Calcolo 21 (1984) 337-352.

[20] M. Fortin and A. Fortin, Experiments with several elements for viscous incompressible flows, Int. J. Num. Meth. Fluids 5 (1985) 911-928.

[21] E.C. Lemmon, Multidimensional integral phase change approximations for finite element conduction codes, Numerical Methods in Heat Transfer, J. Wiley and Sons (1981) 201-214.

[22] W.D. Bennon and F.P. Incropera, A continuum model for momentum, heat and species transport in binary solid-liquid phase change systems – I. Model formulation, Int. J. Heat Mass Transfer 30 (1987) 2161-2170.

[23] C. Prakash and V. Voller, On the numerical solution of continuum mixture equations describing binary solid-liquid phase change, Num. Heat Transfer B 15 (1989) 171-189.

[24] N. Ahmad, Numerical simulation of transport processes in multicomponent systems related to solidification problems, Ph.D. Thesis, Ecole Polytechnique Fédérale de Lausanne (1995).

[25] A.N. Brooks and T.J.R. Hughes, Streamline upwind / Petrov-Galerkin formulations for convection dominated flows with particular emphasis on the incompressible Navier-Stokes equations, Comp. Meth. Appl. Mech. Engrg. 32 (1982) 199-259.

[26] T. Kämpfer, Modeling of macrosegregation using an adaptive domain decomposition method, Ph.D. Thesis, Ecole Polytechnique Fédérale de Lausanne (2002).

[27] W.G. Gray, An efficient finite element scheme for two-dimensional surface water computation, Finite Elements in Water Resources (1977) 4-33.

[28] M.S. Engelman, R.L. Sani and P.M. Gresho, The implementation of normal and/or tangential boundary conditions in finite element code for incompressible fluid flow, Int. J. Num. Meth. Engng. 2 (1982) 225-238.

[29] M. Bellet, Implementation of surface tension with wall adhesion effects in a three-dimensional finite element model for fluid flow, Comm. Num. Meth. Engng. 17 (2001) 563-579.

[30] J.L. Chenot and M. Bellet, The ALE method for the numerical simulation of material forming processes, Proc. Numiform'95, 5th Int. Conf. on Numerical Methods in Industrial Forming Processes, Ithaca, S.-F. Shen and P.R. Dawson (eds.), Balkema, Rotterdam (1995) 39-48.

[31] O. Pironneau, Méthodes des éléments finis pour les fluides (Finite element method for fluid flow), in french, Masson, Paris (1988).

- [32] G. De Vahl Davis and I.P. Jones, Natural convection of air in a square cavity: a comparison exercise, *Int. J. Num. Meth. Fluids* 3 (1983) 227-248.
- [33] G. De Vahl Davis, Natural convection of air in a square cavity: a bench mark numerical solution. *Int. J. Num. Meth. Fluids* 3 (1983) 249-264.
- [34] L. Gaston, Simulation numérique par éléments finis bidimensionnels du remplissage de moules de fonderie et étude expérimentale sur maquette hydraulique (Two-dimensional finite element numerical simulation of the filling of casting moulds and experimental study on a water model), Ph.D. Thesis (in french), Ecole des Mines de Paris (1997).
- [35] H. Combeau, F. Roch, J. C. Chevrier, I. Poitroult and G. Lesoult, Numerical Study of heat and mass transfer during solidification of steel ingots, *Advanced Computational Methods in Heat Transfer*, L. C. Wrobel (ed.), Springer-Verlag, New York (1990) 79-90.
- [36] N. Ahmad, H. Combeau, J.-L. Desbiolles, T. Jalanti, G. Lesoult, M. Rappaz and C. Stomp, Numerical simulation of macrosegregation: a comparison between finite volume method and finite element method predictions and a confrontation with experiments, *Metall. and Mat. Trans.* 29A (1997) 617-630.

Appendix: Definition of conservative normal vectors

The objective of this appendix is to define a set of proper nodal normal vectors, starting from the discretized form of the incompressibility condition. We use then the same reasoning as Gray [27] and Engelman *et al* [28], but extended to three dimensions. In the case of linear spatial interpolation, this will allow us to give a precise expression of conservative nodal normal vectors.

Given $\Omega = \bigcup \Omega_e$ a finite element discretization, a global expression of incompressibility is:

$$\int_{\Omega} \nabla \cdot \mathbf{v} dV = 0 \quad (\text{A1})$$

Injection of the spatial interpolation of the velocity field \mathbf{v} in (A1) yields

$$\int_{\Omega} \frac{\partial N_m}{\partial x_i} V_i^m dV = V_i^m \int_{\Omega} \frac{\partial N_m}{\partial x_i} dV = 0 \quad (\text{A2})$$

where N_m denotes the interpolation function attached to node m , and V_i^m is the component i of the nodal velocity at node m ($i = 1, 3$). Using the gradient theorem, we obtain

$$V_i^m \int_{\partial\Omega} N_m n_i dS = 0 \quad (\text{A3})$$

The summation in (A3) is then restricted to the nodes m belonging to the boundary $\partial\Omega$ of Ω . The integrals of (A2) and (A3) are in fact computed by summation of integrals on the elements Ω_e the node m belongs to. Then (A3) can be cast in the form:

$$\sum_{\substack{\text{boundary} \\ \text{nodes } m}} V_i^m A_i^m = 0 \quad (\text{A4})$$

Following the reasoning of Engelman *et al*, the conservative normal vectors should be such that any tangential nodal velocity (*i.e.* a velocity which is orthogonal to the conservative normal vector) should not contribute to the external flux (A1). Therefore, we should have

$$\text{for any boundary node } m, \quad V_{tg}^m \cdot A^m = 0 \quad (\text{A5})$$

where V_{tg}^m is the tangential velocity vector considered at node m . This means that for each boundary node m , the conservative nodal normal vector $\tilde{\mathbf{n}}^m$ should have the same direction as A^m . Its expression is then given by

$$\tilde{\mathbf{n}}^m = \frac{1}{\|A^m\|} A^m \quad (\text{A6})$$

$$\text{with } A_i^m = \int_{\partial\Omega} N_m n_i dS \quad (\text{A7})$$

In the specific case of a linear discretization, (A7) reduces to

$$A_i^m = \sum_{e \in \tau(m)} \frac{1}{3} n_i^e S^e \quad (\text{A8})$$

where $\tau(m)$ denotes the set of triangular facets surrounding node m , \mathbf{n}^e is the normal vector to facet e and $1/3$ is the value of the interpolation function attached to the node m at the centre of each surrounding facet. Finally, the conservative normal vector at node m is the average of the normals of the surrounding facets weighted by their surface:

$$\tilde{\mathbf{n}}^m = \frac{1}{\left\| \sum_{e \in \tau(m)} \mathbf{n}^e S^e \right\|} \sum_{e \in \tau(m)} \mathbf{n}^e S^e \quad (\text{A9})$$

	$Ra = 10^3$		$Ra = 10^4$	
	De Vahl Davis and Jones	Present solution	De Vahl Davis and Jones	Present solution
$\max(v_x)$	3.649	3.634	16.178	16.099
z	0.813	0.811	0.823	0.814
$\max(v_z)$	3.697	3.669	19.617	19.413
x	0.178	0.183	0.119	0.108

Table 1: Maximum values of velocity components for the square cavity test (De Vahl Davis and Jones [32-33]).

Thermal conductivity	$30 \text{ W.m}^{-1}.\text{K}^{-1}$
Specific heat	$500 \text{ J.kg}^{-1}.\text{K}^{-1}$
Latent heat of fusion	$3.09 \cdot 10^5 \text{ J.kg}^{-1}$
Melt temperature	$1538 \text{ }^\circ\text{C}$
Liquidus line slope	$-80 \text{ K (wt\%C)}^{-1}$
Partition coefficient	0.18
Thermal expansion coefficient	$2.95 \cdot 10^{-5} \text{ K}^{-1}$
Solutal expansion coefficient	$1.42 \cdot 10^{-2} (\text{wt\%C})^{-1}$
Reference temperature	$1523 \text{ }^\circ\text{C}$
Reference concentration in liquid	0.2 wt%C
Reference density	7060 kg.m^{-3}
Dynamic viscosity	$4.2 \cdot 10^{-3} \text{ Pa.s}$
Secondary dendrite arm spacing	10^{-4} m
Heat convection coefficient (h)	$100 \text{ W.m}^{-2}.\text{K}^{-1}$
External temperature (T_{ext})	$20 \text{ }^\circ\text{C}$

Table 2. Material and other physical data for the macrosegregation test.

Figure captions

Fig. 1. P1+/P1 element.

Fig. 2. ALE formulation: schematic in two dimensions. Updating of the location of a finite element node and subsequent identification of the upwind element. The materialization of the trajectory of two material particles *A* and *B* helps in the interpretation of equation (51).

Fig. 3. Illustration of transport procedure by use of a pseudo Lagrangian update and direct interpolation.

Fig. 4. Lagrangian and Eulerian-Lagrangian nodes, as determined by their belonging to solid-like and liquid-like finite elements. Schematic in two dimensions.

Fig. 5. Water model. Experimental set-up.

Fig. 6. Water model. Comparison between experimental flow and turbulent finite element computation.

Fig. 7. Thermal conditions for the macrosegregation test problem and 3D finite-element mesh.

Fig. 8. Macrosegregation patterns at 1000 s, computed by SOLID and THERCAST[®].

Fig. 9. Geometry of the cast part (dimensions in mm) and finite element mesh of the casting and of the six different subdomains of the mould.

Fig. 10. Computation of the pipe formation. Iso-values of the liquid fraction.

Fig. 11. Comparison of calculated (left) and measured (right) shapes of the pipe. The section plane is the longitudinal mid plane of the part.

Fig. 12. Illustration of the advancement of the solidification of the ingot:

- a) Initial configuration and finite element meshes
- b) velocity field at 1 min (max velocity 34.7 mm/s)
- c) velocity field and iso-liquid fraction (from red or dark grey = 1 to blue or light grey = 0) at 10 min (max velocity 5.6 mm/s)
- d) velocity field and iso-liquid fraction at 30 min (max velocity 5.4 mm/s)
- e) velocity vectors and liquid-like (blue or light grey) and solid-like (red or dark grey) elements at 1 h (max velocity 9.7 mm/s)
- f) velocity vectors, liquid-like and solid-like elements, and isolines of liquid fraction (8 lines between 0.2 and 0.8, maximum 0.98) at 2 h 30 min (max velocity 0.55 mm/s)

Fig. 13. Formation of the gap at the shoulder of the ingot.

- a) Iso-temperatures (915 °C in the ingot corner), isolines of liquid fraction (min = 0 in the corner ; 8 lines with a spacing of 0.11, max = 1), and velocity vectors (maximum 2.5 mm/s in this region) after 8 min.
- b) Iso-temperatures (800 °C in the corner) at 2 h 30 min.
- c) Configuration at the end of solidification (3h 16 min).

Fig. 14. Air gap formation due to solidification shrinkage at the bottom of the ingot. Solid-type elements are in red or dark grey. Velocity vectors are shown as well as isolines of liquid fraction (8 lines, spacing 0.11 ; min = 0, max = 1).

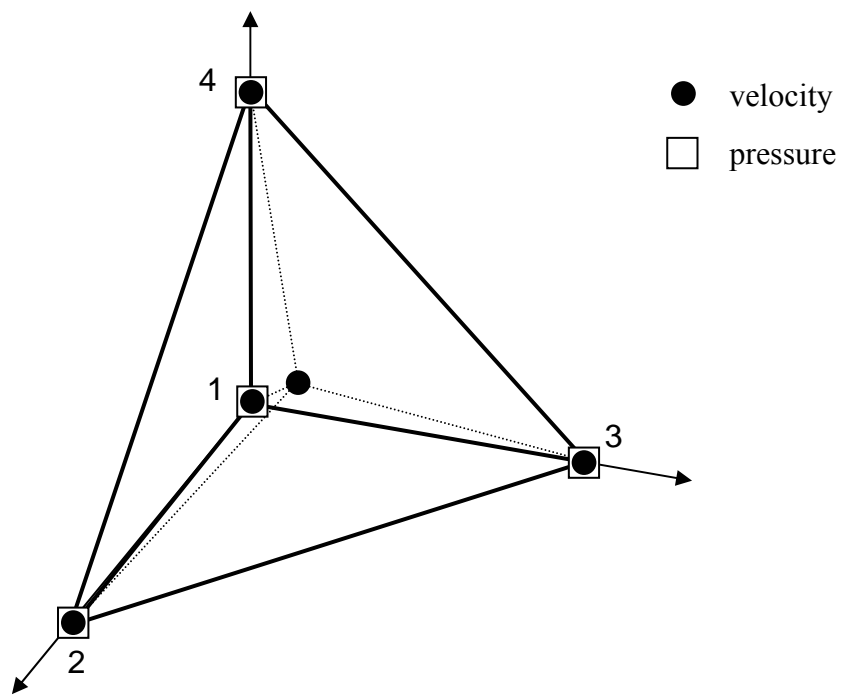


Fig. 1. P1+/P1 element.

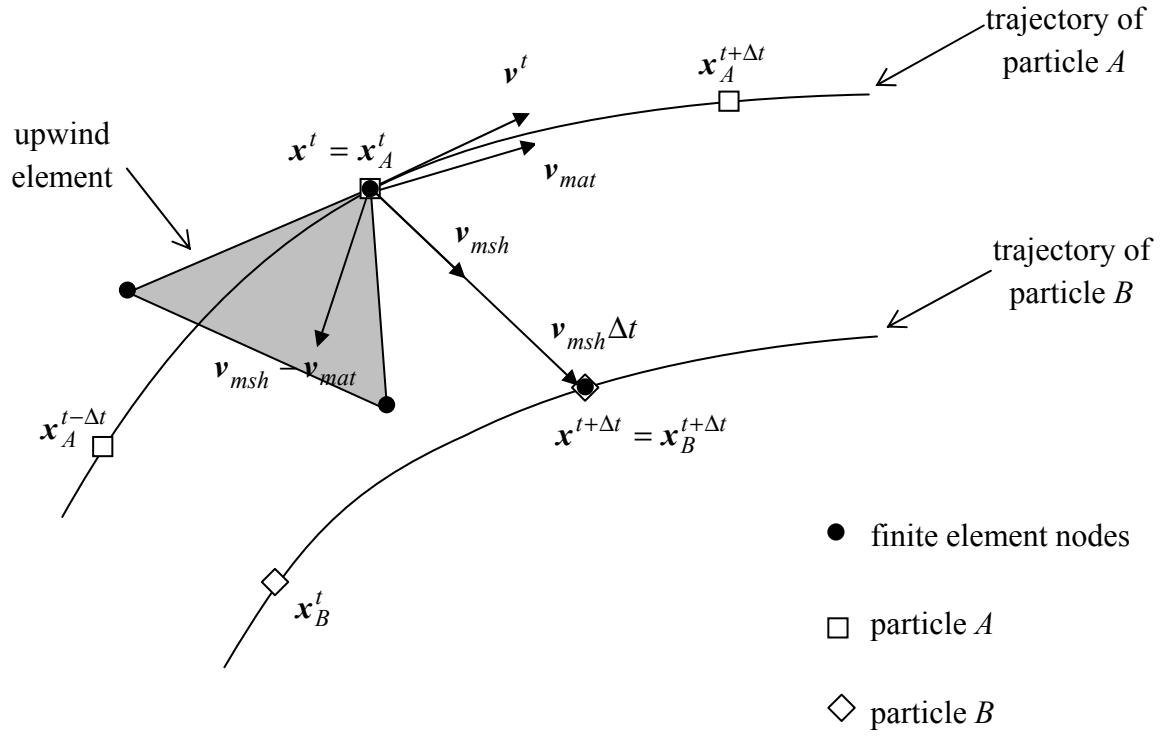


Fig. 2. ALE formulation: schematic in two dimensions. Updating of the location of a finite element node and subsequent identification of the upwind element. The materialization of the trajectory of two material particles A and B helps in the interpretation of equation (51).

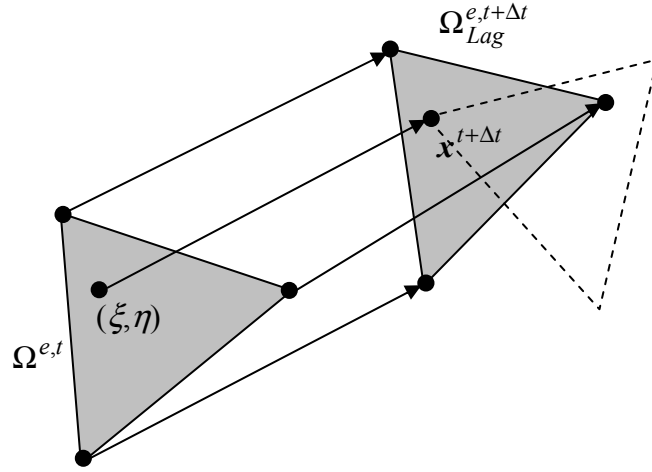


Fig. 3. Illustration of transport procedure by use of a pseudo Lagrangian update and direct interpolation.

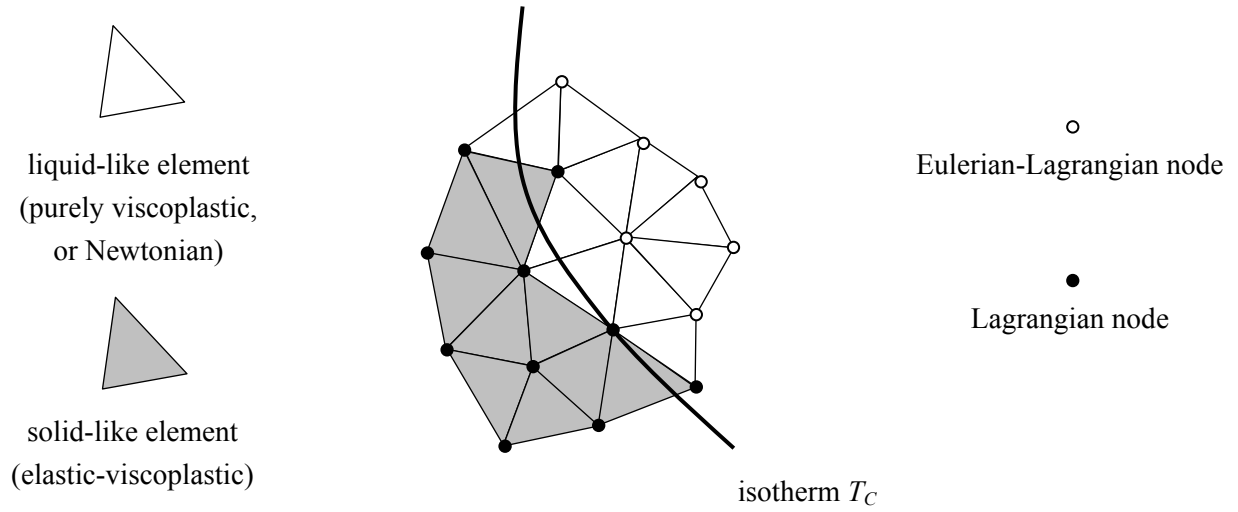


Fig. 4. Lagrangian and Eulerian-Lagrangian nodes, as determined by their belonging to solid-like and liquid-like finite elements. Schematic in two dimensions.

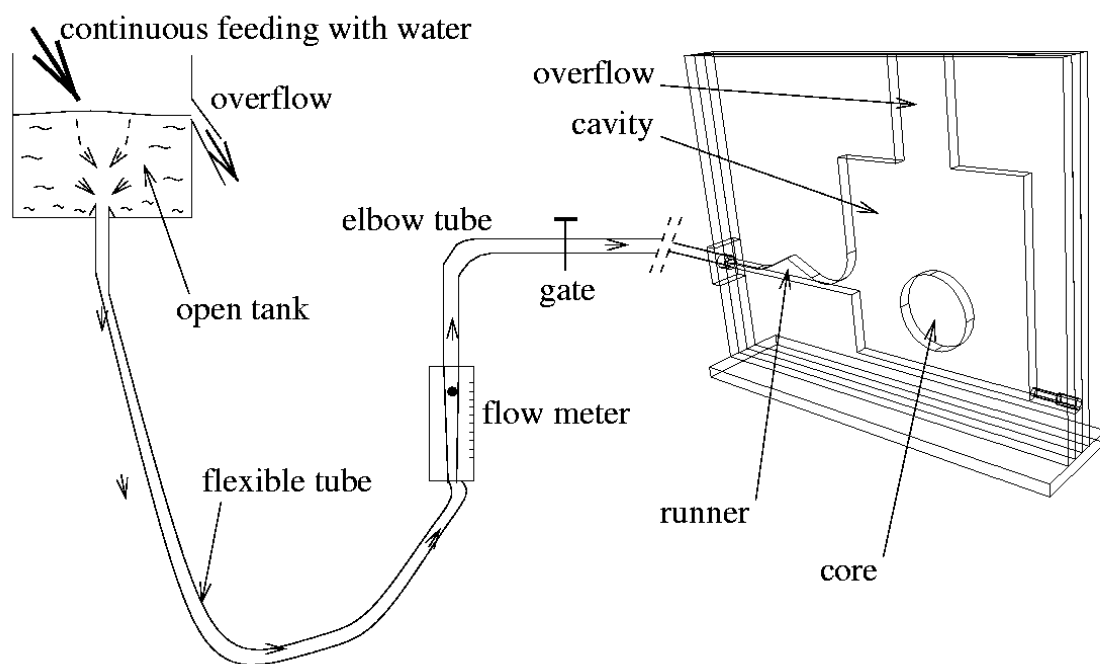


Fig. 5. Water model. Experimental set-up.

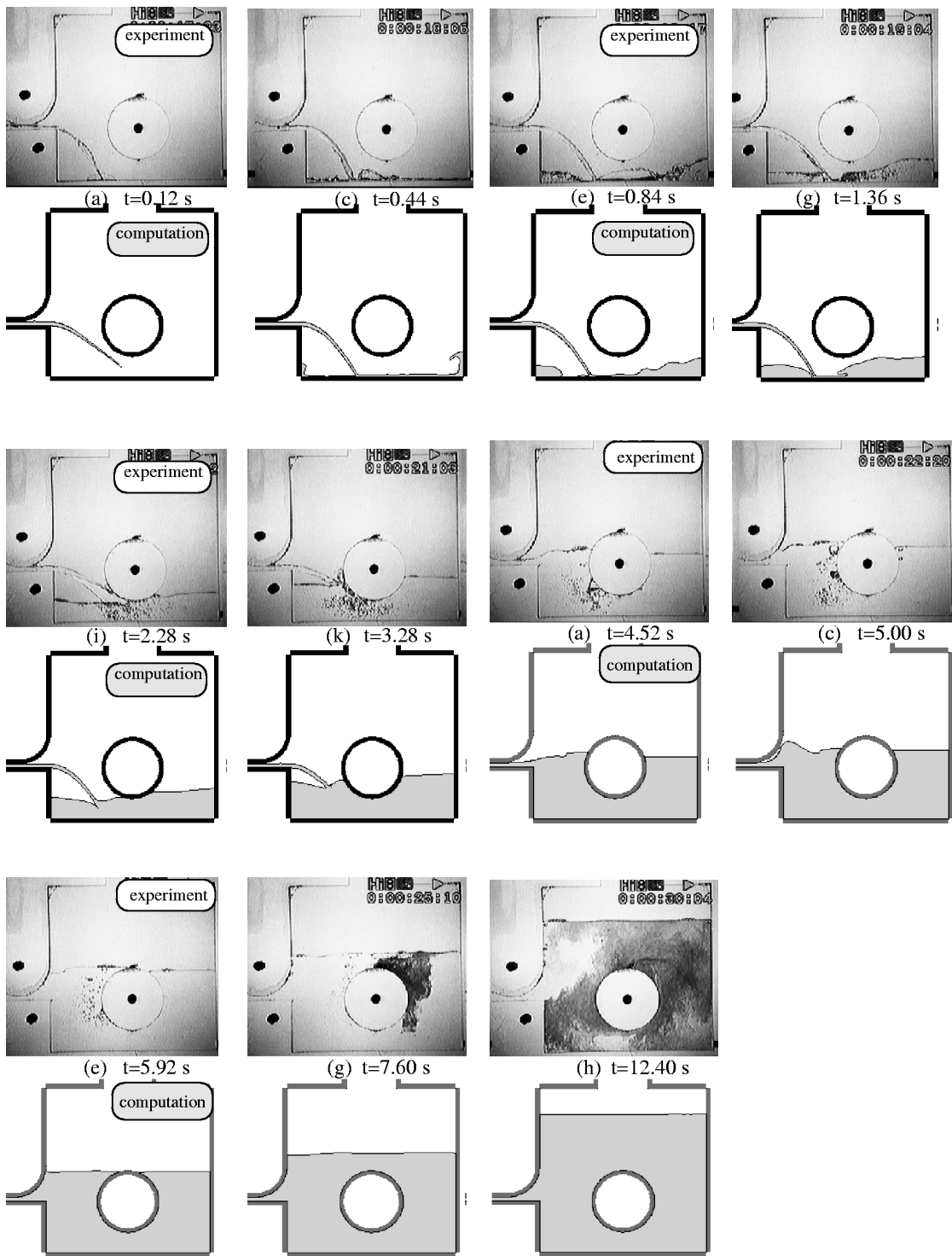


Fig. 6. Water model. Comparison between experimental flow and turbulent finite element computation.

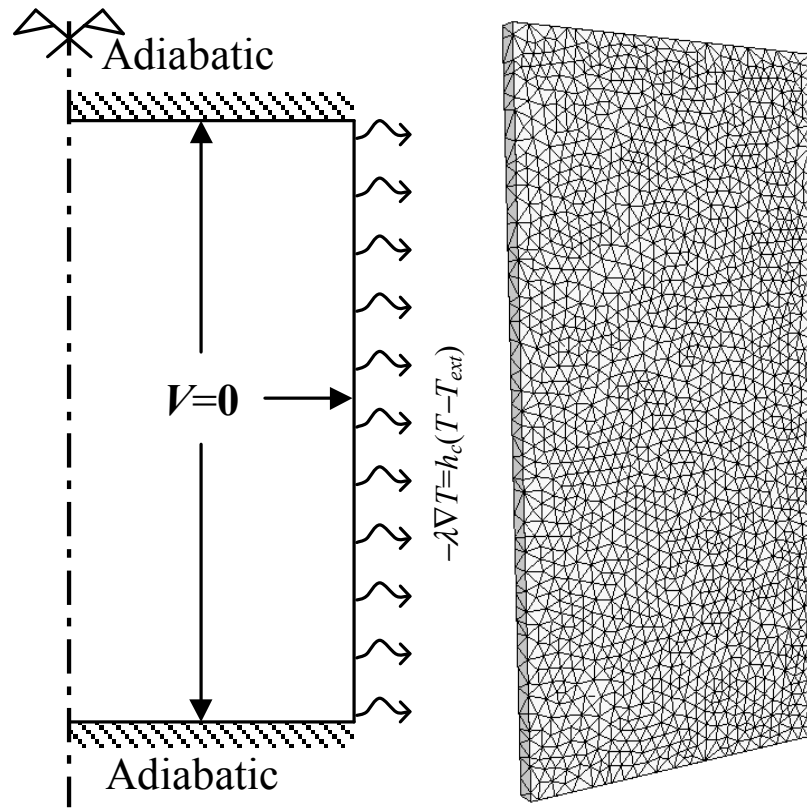


Fig. 7. Thermal conditions for the macrosegregation test problem and 3D finite-element mesh.

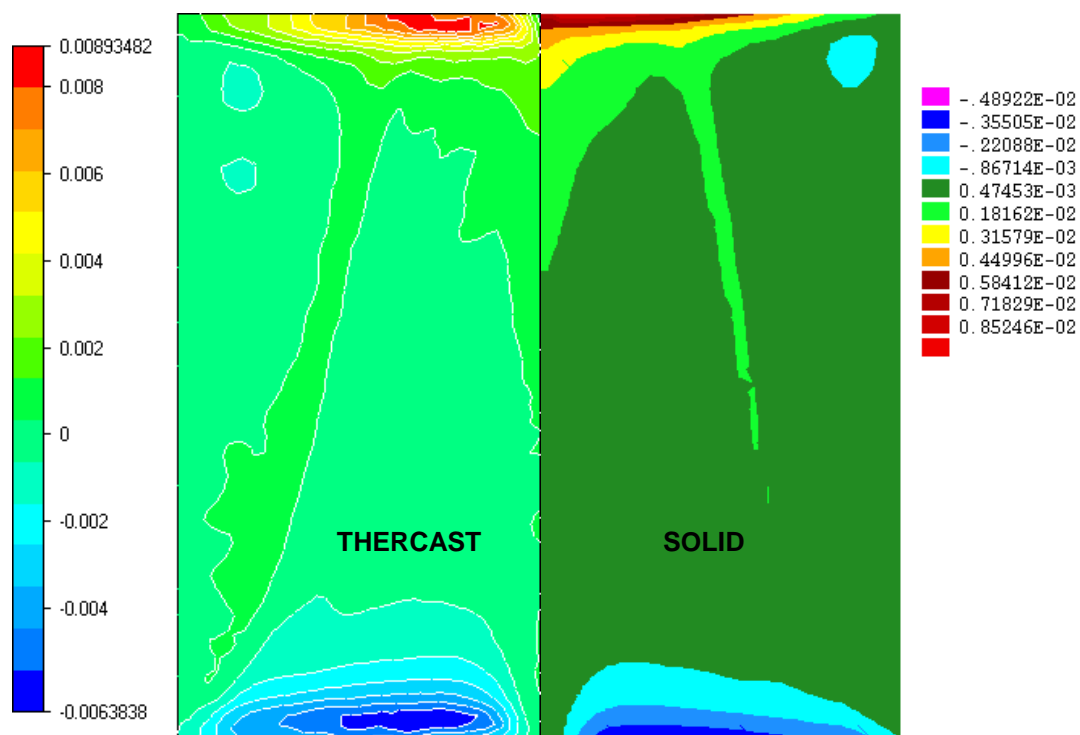


Fig. 8. Macrosegregation patterns at 1000 s, computed by SOLID and THERCAST®.

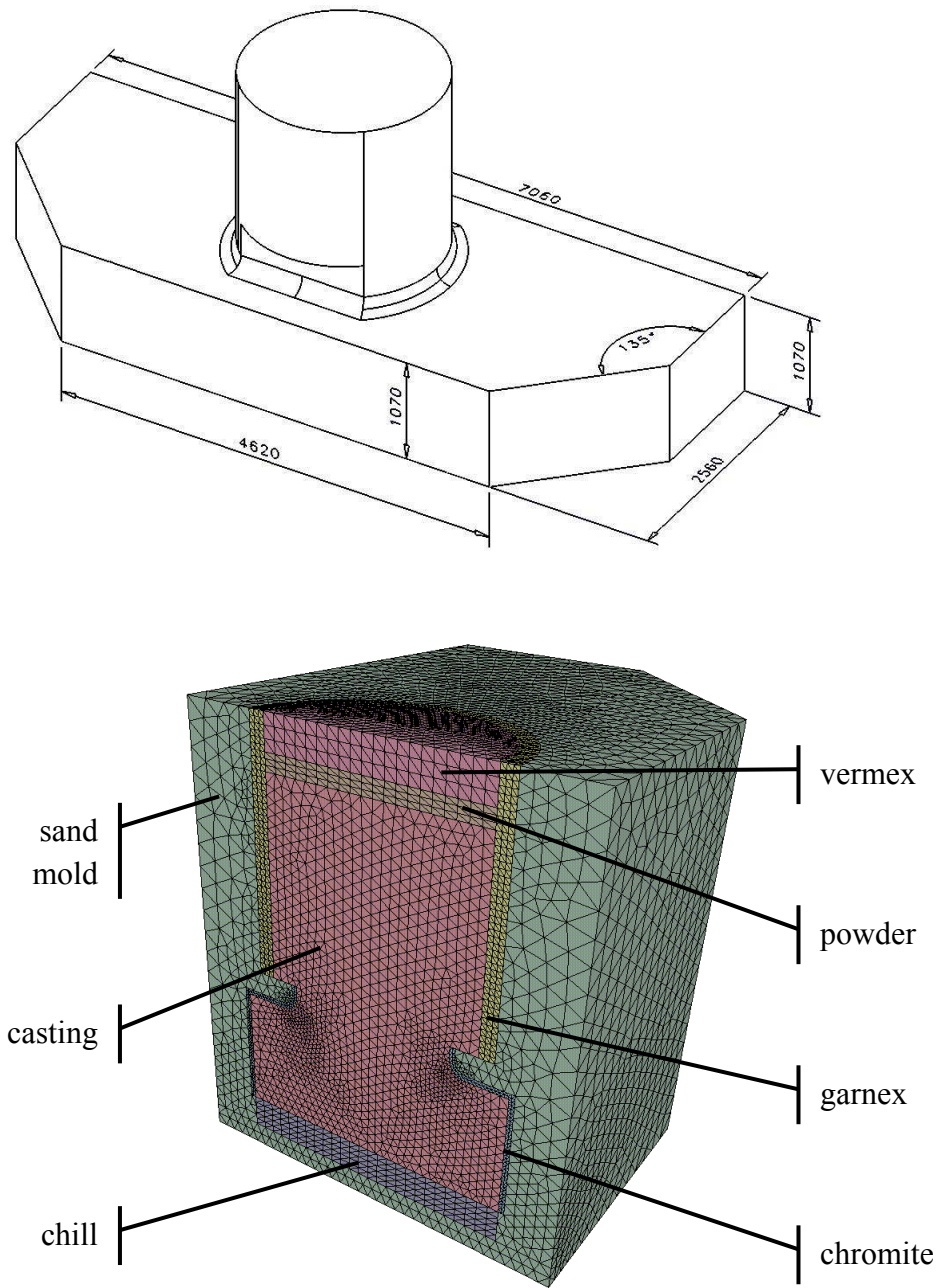


Fig. 9. Geometry of the cast part (dimensions in mm) and finite element mesh of the casting and of the six different subdomains of the mould.

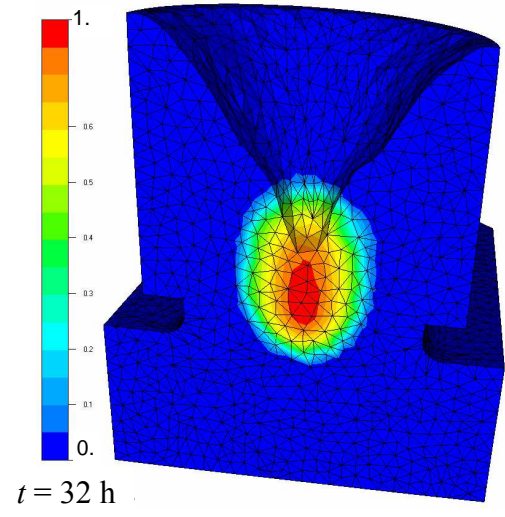
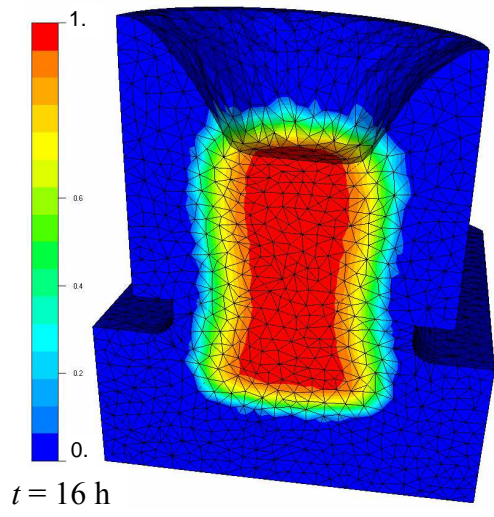
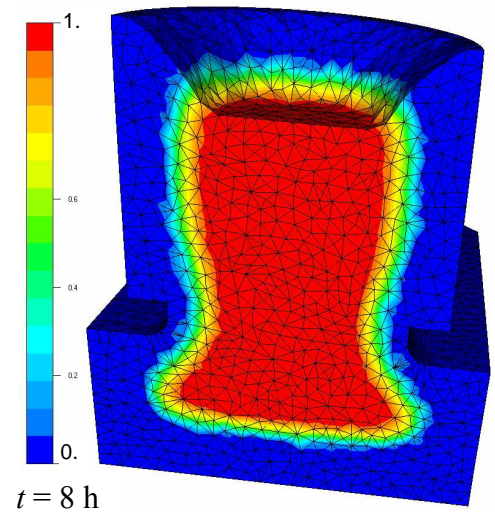
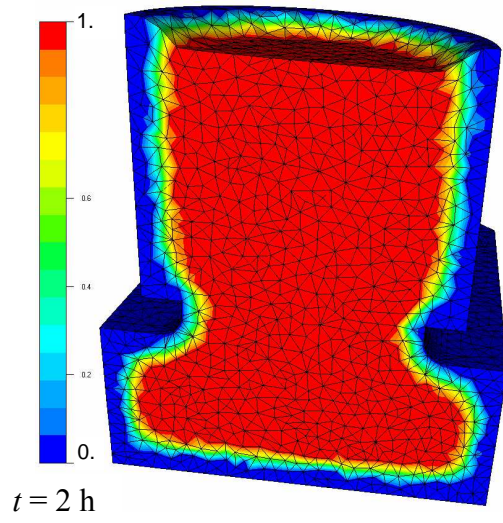
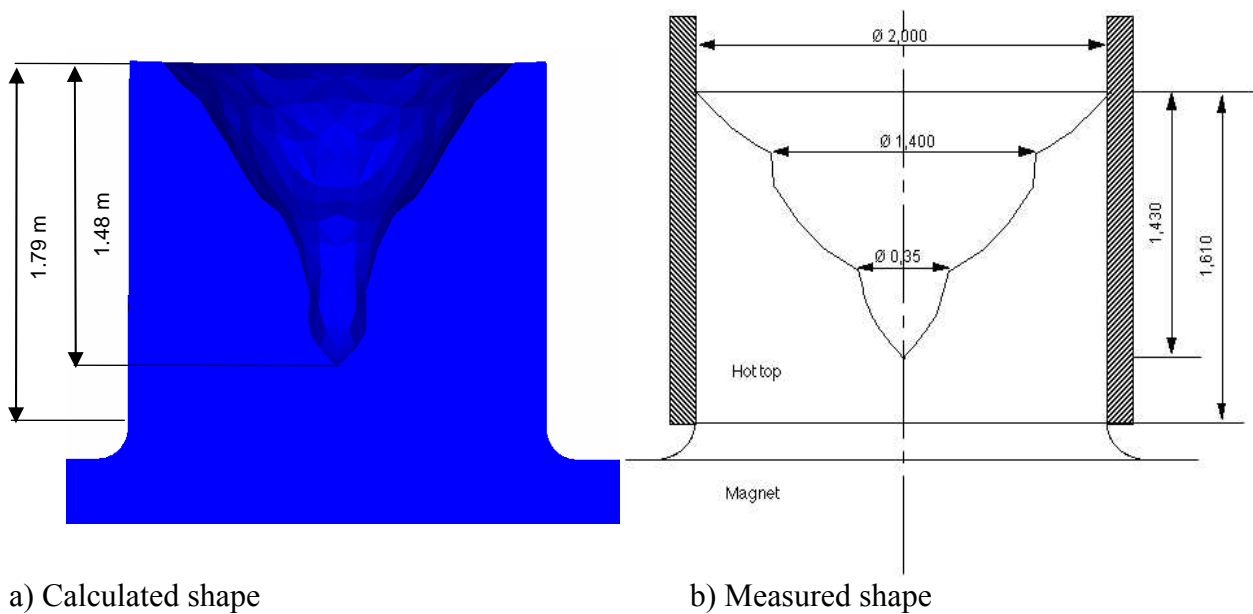


Fig. 10. Computation of the pipe formation. Iso-values of the liquid fraction.



a) Calculated shape

b) Measured shape

Fig. 11. Comparison of calculated (left) and measured (right) shapes of the pipe. The section plane is the longitudinal mid plane of the part.

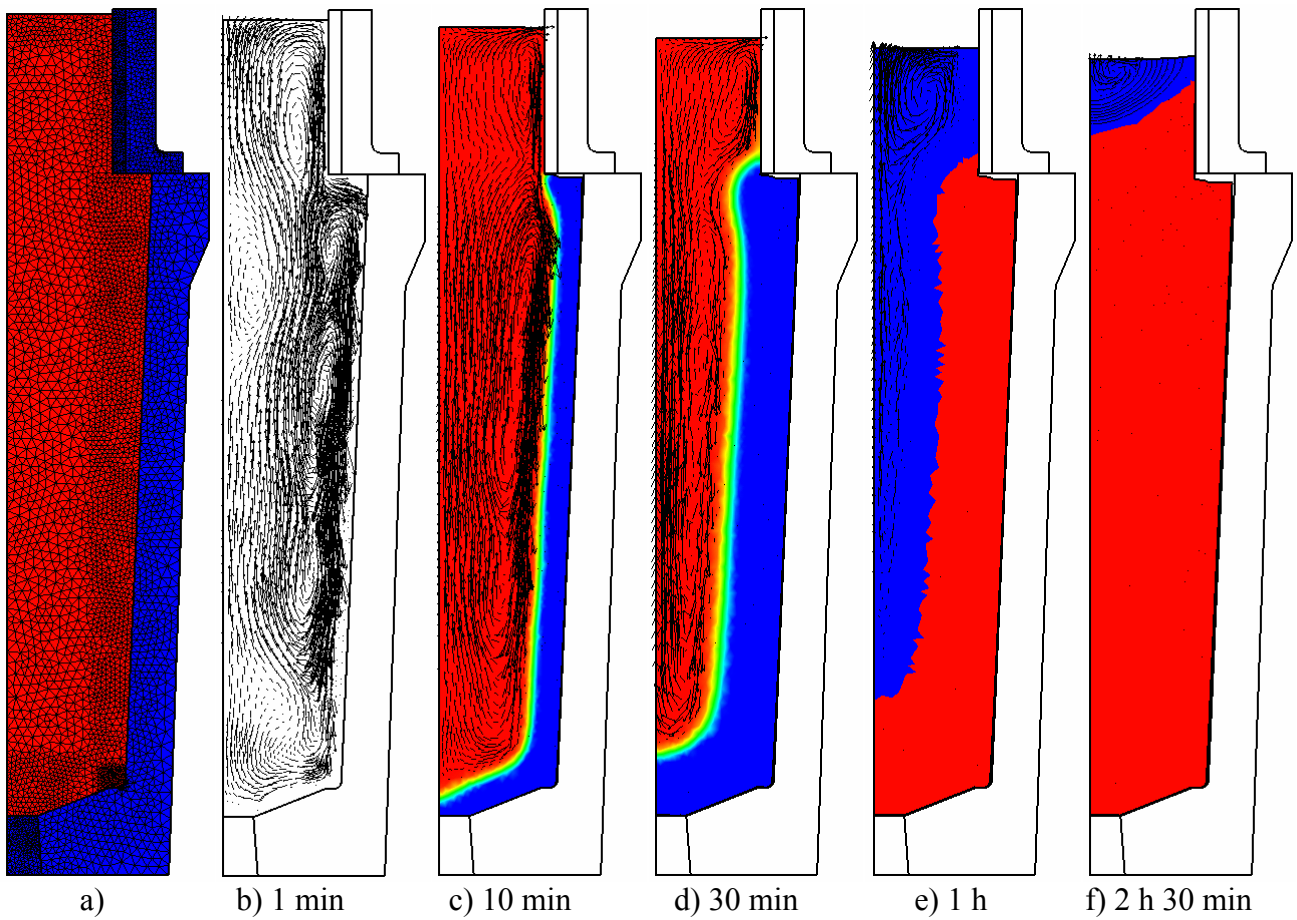


Fig. 12. Illustration of the advancement of the solidification of the ingot:

- a) Initial configuration and finite element meshes
- b) velocity field at 1 min (max velocity 34.7 mm/s)
- c) velocity field and iso-liquid fraction (from red or dark grey = 1 to blue or light grey = 0) at 10 min (max velocity 5.6 mm/s)
- d) velocity field and iso-liquid fraction at 30 min (max velocity 5.4 mm/s)
- e) velocity vectors and liquid-like (blue or light grey) and solid-like (red or dark grey) elements at 1 h (max velocity 9.7 mm/s)
- f) velocity vectors, liquid-like and solid-like elements, and isolines of liquid fraction (8 lines between 0.2 and 0.8, maximum 0.98) at 2 h 30 min (max velocity 0.55 mm/s)

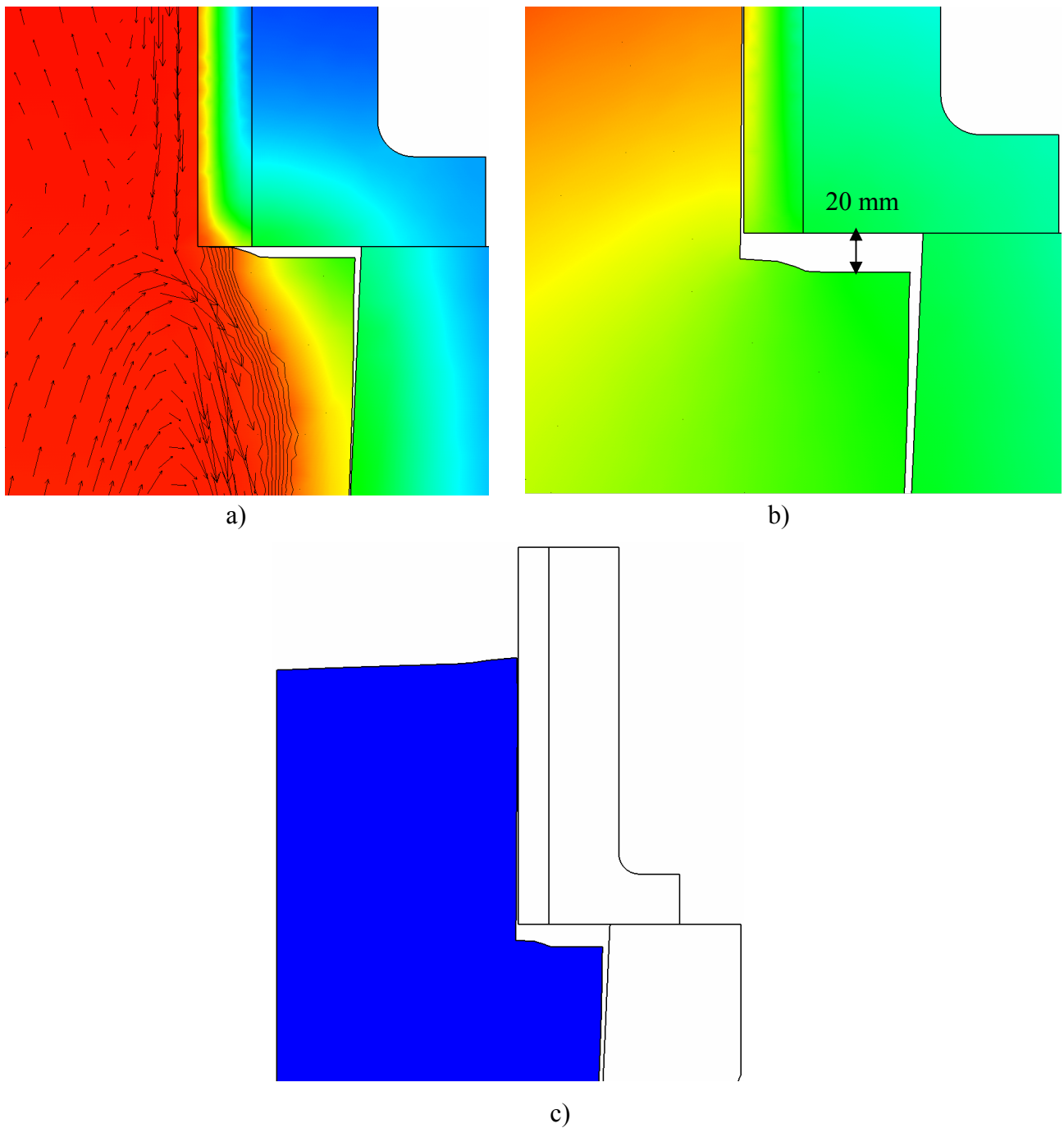


Fig. 13. Formation of the gap at the shoulder of the ingot.

- a) Iso-temperatures (915 °C in the ingot corner), isolines of liquid fraction (min = 0 in the corner ; 8 lines with a spacing of 0.11, max = 1), and velocity vectors (maximum 2.5 mm/s in this region) after 8 min.
- b) Iso-temperatures (800 °C in the corner) at 2 h 30 min.
- c) Configuration at the end of solidification (3h 16 min).

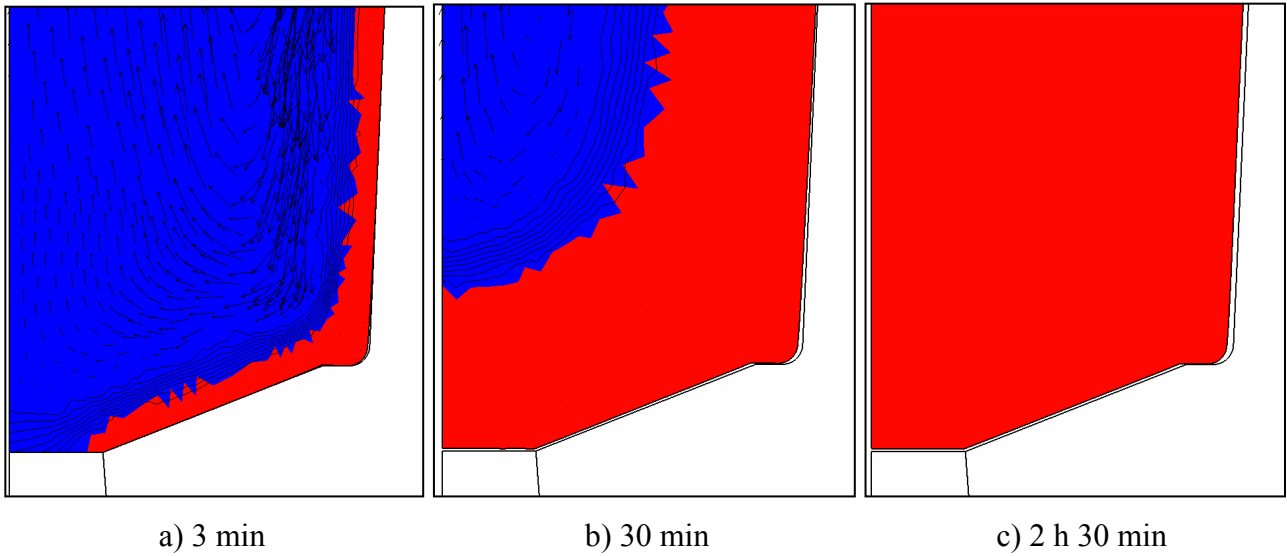


Fig. 14. Air gap formation due to solidification shrinkage at the bottom of the ingot. Solid-type elements are in red or dark grey. Velocity vectors are shown as well as isolines of liquid fraction (8 lines, spacing 0.11 ; min = 0, max = 1).

